Czech Technical University
in Prague

Faculty of Nuclear Sciences and Physical
Engineering

Department of Physics

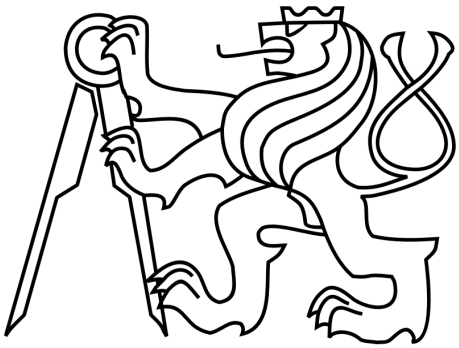

Master's Thesis

Image and scintillator data analysis in the AEgIS experiment

Bc. Alena Zemanová

Supervisor: doc. RNDr. Vojtěch Petráček, CSc.

Prague, 2019

České vysoké učení technické
v Praze

Fakulta jaderná a fyzikálně inženýrská

Katedra fyziky

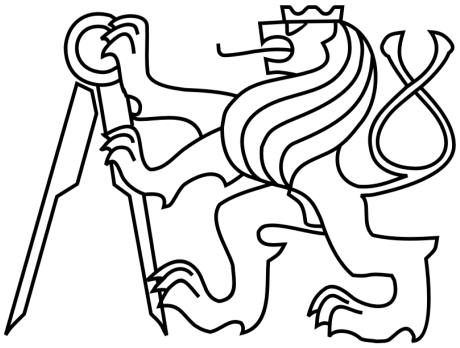

Diplomová práce

Analýza obrazu a dat z externích scintilátorů v experimentu AEgIS

Bc. Alena Zemanová

Vedoucí práce: doc. RNDr. Vojtěch Petráček, CSc.

Praha, 2019

Declaration:

I hereby declare that this project is the result of my own work and all the sources I used are in the list of references.

I have no objection to usage of this work in compliance with the act §60 Law No. 121/2000 Coll. (Copyright Act), and with the rights connected with the copyright act including the changes in the act.

Čestné prohlášení:

Prohlašuji, že jsem tuto práci vypracovala samostatně a použila jsem pouze podklady (literaturu, projekty, SW, atd.) uvedené v přiloženém seznamu.

Nemám závažný důvod proti užití tohoto školního díla ve smyslu § 60 Zákona č. 121/2000 Sb., o právu autorském, o právech souvisejících s právem autorským a o změně některých zákonů (autorský zákon).

V Praze dne ....

Bc. Alena Zemanová

Title: **Image and scintillator data analysis in the AEgIS experiment**

Author: Bc. Alena Zemanová

Department: Department of Physics FNSPE CTU in Prague
Branch of study: Experimental Nuclear and Particle Physics
Kind of thesis: Master's thesis

Supervisor: doc. RNDr. Vojtěch Petráček, CSc.

Abstract: Whilst the validity of the Weak Equivalence Principle (WEP) has been demonstrated to a high precision with normal matter, it has yet to be tested to such a rigorous degree for antimatter. Testing the WEP for antimatter forms the primary scientific goal of the AEgIS experiment, which seeks to directly measure the Earth's local gravitational acceleration g on a neutral antihydrogen beam. The production mechanism chosen by the collaboration is a resonant charge-exchange between the antiproton plasma and a cloud of excited Rydberg Ps atoms. Before the measurement can be performed however, an effective means of producing antihydrogen is required.

This thesis presents a technical overview of the steps taken to produce antihydrogen, as well as a description of the experimental apparatus comprising AEgIS. The key findings of the experiment are summarised, and the future direction of the collaboration is examined. The remainder of the thesis is concerned with image and scintillator data analysis. Specifically, results for image refinement via deconvolution are presented and discussed.

Keywords: antimatter, antihydrogen, deconvolution of the image, experiment AEgIS, resonant charge-exchange

Název práce: **Analýza obrazu a dat z externích scintilátorů experimentu AEgIS**

Autor: Bc. Alena Zemanová

Katedra: Katedra fyziky FJFI ČVUT v Praze
Studijní obor: Experimentální jaderná a částicová fyzika
Druh práce: Diplomová práce

Vedoucí práce: doc. RNDr. Vojtěch Petráček, CSc.

Abstrakt: Jeden z mnoha testů, které byly velmi přesně změřeny pro hmotu, ale nikoliv pro antihmotu, je takzvaný princip slabé ekvivalence, který je velmi úzce spojen s měřením gravitační interakce. Prvotním fyzikálním cílem experimentu AEgIS je přímé změření gravitačního zrychlení g neutrálního antivodíkového svazku, a tedy potvrzení tohoto principu. Produkční mechanismus, který byl kolaborací vybrán, se nazývá rezonantní nábojová výměna mezi antiprotonovým plazmatem a vysoce excitovanými atomy pozitronia. K úspěšnému provedení tohoto měření je potřeba efektivní tvorby antivodíkových atomů.

Tato diplomová práce shrnuje všechny kroky, které byly uskutečněny k úspěšné produkci antivodíku, společně se samotným produkčním mechanismem. Částí práce je také detailní popis celé experimentální aparatury. Na konci práce je provedeno vylepšení jedné z diagnostických částí experimentu, dekonvoluce obrazu z Micro-Channel Plate.

Klíčová slova: antihmota, antivodík, dekonvoluce obrazu, experiment AEgIS, rezonantní nábojová výměna

Poděkování:

Na tomto místě bych chtěla poděkovat především svému školiteli doc. RNDr. Vojtěchu Petráčkovi, CSc. za jeho vstřícnost, trpělivost a ochotu, kterou prokazoval po celou dobu naší spolupráce. Také bych mu chtěla poděkovat za příležitost pracovat v mezinárodním kolektivu experimentu AEgIS, a to včetně možnosti pracovat přímo v místě, kde je experiment postaven, tedy v CERNu.

Také bych chtěla poděkovat všem svým spolužákům a kamarádům za jejich podporu a cenné rady během celého studia, a to jak ve školních lavicích, tak i mimo ně.

V neposlední řadě bych chtěla poděkovat své rodině za zázemí a nepřetržitou podporu.

My thanks also goes to the people in the AEgIS collaboration. Thank you for all the answers to my questions and for the patience during the time spent with me when I tried to understand the experimental apparatus. Thank you for all the lovely time I have spent in CERN, for all the chocolate bars, which were always available in the control room and also for the support during (sometimes endless) shifts.

Last but not the least a big thank you goes to a very special person who helped me during the last months during the time of writing this thesis. Thank you once again.

Contents

List of Figures

Introduction

Since its prediction by Dirac at the beginning of the 20th century, and its experimental discovery in 1933 by Anderson, antimatter has been the object of many studies; including tests on QED theory, the Charge, Parity and Time Reversal (CPT) theorem and also its basic properties in order to compare it with ordinary matter.

One of the tests, which has been confirmed with matter, but not with antimatter is proof of the theorem of the Weak Equivalence Principle (WEP), which is closely connected to measuring gravity.

In order to investigate this theorem, three independent groups were established - the GBAR experiment, the ALPHA-g project and the AEgIS experiment - Antihydrogen Experiment: Gravity, Interferometry, Spectroscopy.

Of the three aforementioned groups, this thesis will focus on the latter. AEgIS aims to measure the gravitational acceleration of cold antihydrogen atoms. These atoms are produced by a charge-exchange process between trapped antiproton plasma and a cloud of excited Rydberg positronium atoms.

In this thesis, the main steps towards this production of antihydrogen are investigated together with the analysis of the image from the micro-channel plate, which is one of the crucial diagnostic tools in the experiment.

The first chapter is dedicated to the theoretical background of the experiment - specifically, to the Weak Equivalence Principle and prior tests of it throughout history.

In the second chapter, the apparatus of the AEgIS experiment is introduced. At first, the Antiproton Decelerator, the only source of cold antiprotons in the world, is described together with the principle of antiproton production and the antiproton cooling inside the decelerator. Next, the layout of the AEgIS experiment is described together with its detection system and particle diagnosis. Also, the future of the experiment is briefly discussed. Then, two main parts of the AEgIS apparatus are described in detail - the positron apparatus and the main trap system, which is the most important part for the antihydrogen production.

In the third chapter, different types of antihydrogen production are summarised. At the beginning, the production of fast antihydrogen atoms is described, together with the first production of antihydrogen atoms ever. After that, two examples of production of cold antihydrogen atoms are given - three-body recombination and resonant charge-exchange.

In the fourth chapter, the summary of 2018 beamtime at the AEgIS experiment, which was dedicated to the antihydrogen production, is presented. At the beginning, the manipulations of antiprotons - loading, cooling, stacking and compression - is described in detail. In the second part of the chapter, the antihydrogen production and detection are described.

Finally, in the fifth and final chapter, the image analysis from the micro-channel plate (MCP) is presented. At the beginning, the term deconvolution of the image is introduced together with the Richardson-Lucy algorithm. At the end of the chapter, results obtained by using this method are shown.

Chapter 1

Why is Measuring Gravity So Important?

The primary scientific goal of the AEgIS experiment is to directly measure the Earth's local gravitational acceleration g on neutral antimatter atoms, $\bar{\mathrm{H}}$. This measurement is closely connected to the testing of the principle of universality of the free-fall, which is a consequence of the more general Equivalence Principle (EP). In this chapter, the basics of the EP will be explained together with its tests, which have been already taken.

1.1 The equivalence principle

Although gravity is known since Galileo's observation and antimatter is known since the 1930s, there were no tests which would prove gravity properties of antimatter yet. Scientists have to struggle with problems, which antimatter brings: firstly, antimatter itself is very rare (and mostly also unstable) material. Secondly, most of the stable antimatter are charged particles (antiprotons, positrons), which makes the measurement almost impossible since the gravity force is the weakest of all fundamental interactions. The studies of gravitational behaviour of charged antiparticles would need both electrical and magnetic fields to be screened out with a precision of 10^{-36} at least, which is unachievable. Due to this fact, the only way how to study this kind of behaviour is to use electrically neutral antimatter particles (with small initial velocities).

The principle of universality of the free-fall begins with Newtonian physics terms, which require the exact equivalent between inertial (m_i - from the second Newton's law) and gravitational masses (m_g - from the first Newton's law), $m_i = m_g$.

Now is gravity described by Einstein's general relativity with a more general equivalence principle as its foundation. This Equivalence Principle (EP) states: *a homogeneous*

gravitational field is locally equivalent to a uniformly accelerated reference frame, with a prediction from the Universality of Free Fall (UFF): *the trajectory of a point object freely falling in a gravitational field depends only on the object's initial condition and not on its composition* [1].

From an experimental point of view is customary to distinguish two forms of the EP: Strong and Weak. The Strong Equivalence Principle (SEP) states that all interactions (including gravity) give equal contributions to $m_i = m_g$. On the other hand, the Weak Equivalence Principle (WEP) neglect the gravity contributions, which means that the falling objects are bound by non-gravitational forces.

A review of the main experiments which set the boundary for SEP and WEP follows.

1.1.1 EP for matter

Although there are no experimental tests for antimatter yet, the Equivalence Principle was tested very successfully during the last century with matter systems.

The fact, that the experiments use very different systems (an overview can be seen in [2]) leads to introducing a comparing parameter η, that measures the strength of the EP-violation. This parameter is known as the Eötvös parameter and it is defined as the difference of the acceleration of two examined bodies divided by the average:

$$\eta = \frac{|a_1 - a_2|}{|a_1 + a_2|/2}, \tag{1.1}$$

in terms of masses:

$$\eta = 2\frac{|(m_g/m_i)_1 - (m_g/m_i)_2|}{|(m_g/m_i)_1 + (m_g/m_i)_2|/2}. \tag{1.2}$$

Bounds on η for SEP

The installation of the corner cube retro-reflectors on the lunar surface more than 35 years ago with the Apollo 11 lunar landing, initiated a unique program of lunar laser ranging (LLR) tests of the EP. LLR accurately measures the round-trip time of flight for a laser pulse fired from an observatory on the Earth, bounced off of a corner cube retro-reflector on the Moon, and returned to the observatory. [3]

The SEP result from this kind of experiments is

$$\left[\left(\frac{m_g}{m_i}\right)_{Earth} - \left(\frac{m_g}{m_i}\right)_{Moon}\right]_{SEP} = (-2.0 \pm 2.0) \cdot 10^{-13}, \tag{1.3}$$

which can be translated into a value for the corresponding SEP violation parameter

$$\eta_{strong} = (4.4 \pm 4.5) \cdot 10^{-4}.$$

Bounds on η for WEP

As can be seen from Figure 1.1 many tests were taken to measure the Eötvös parameter (η) precisely.

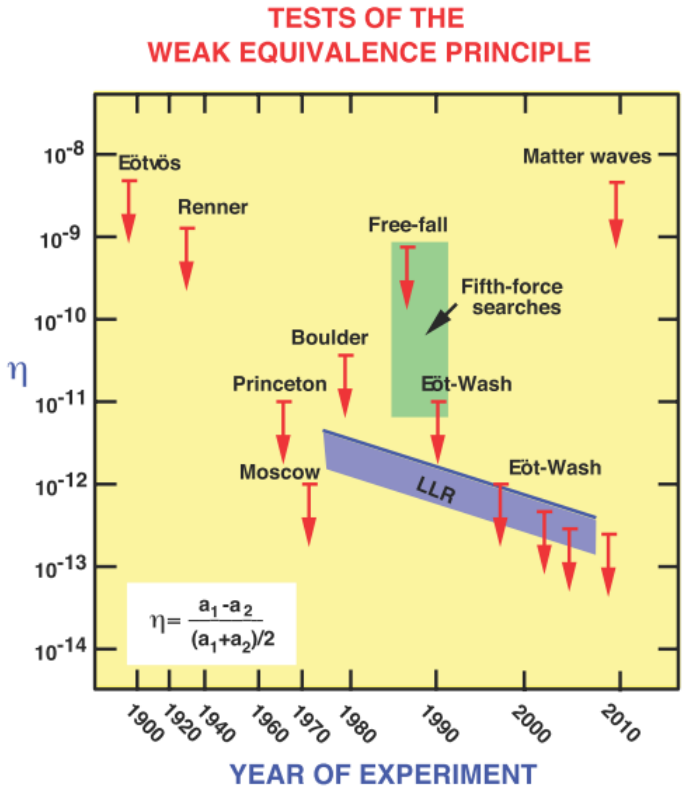

Figure 1.1: Tests of the WEP taken until 2010. The Eötvös parameter η versus the year of the test is plotted. Taken from [2].

The first test was taken during the 17th century by Galileo, Newton and Bessel with two oscillating pendulums of different compositions, concerning the fact that the two masses are in free fall along the tangent to the trajectory of their respective oscillation. The precision reached by this experiment was $\eta < 10^{-3}$. Later were these tests improved to reach the precision 10^{-5}.

These results were considered as the most precise ones until 1890 when Eötvös published the first results of his test of the equivalence principle with a precision $\eta < 10^{-8}$. Eötvös experiment is called torsion balance experiment an its principle can be described by Einstein's words: *A body on the surface of the Earth is acted upon by the terrestrial*

gravitation and the centrifugal force. The gravitational mass is the determining factor for the first force and the inertial mass for the second one. If the two did not coincide, then the direction of the resultant of the two (apparent gravitation) would depend on the material of which this body consists. [4] The sketch of the principle can be seen in Figure 1.2.

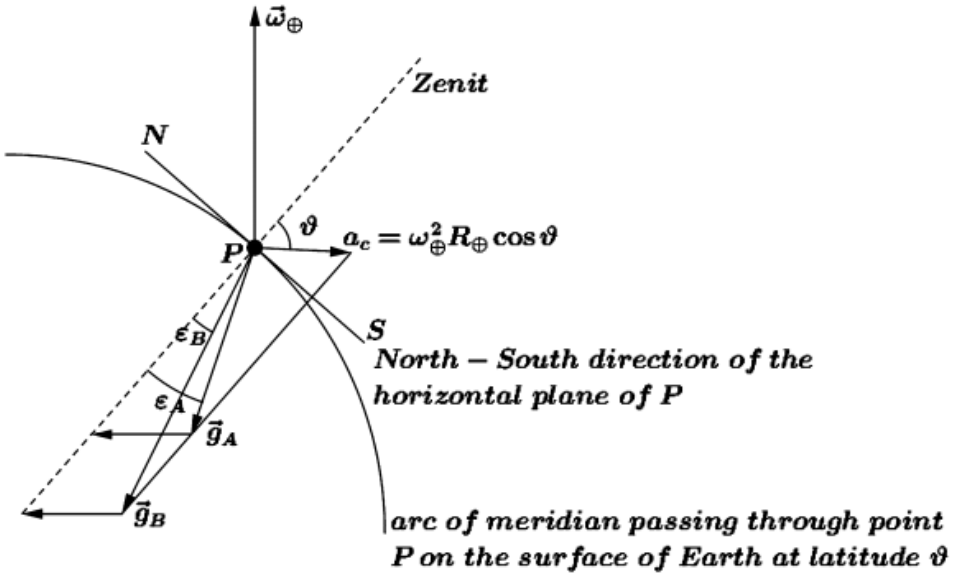

Figure 1.2: The principle of torsion balance experiment. Two plumbs lines in P, at latitude θ on the surface of the Earth rotating with angular velocity $\vec{\omega}$, have masses of different composition, A and B. We assume them to have the same inertial mass m_i, but different gravitational masses: $m_A^g = m_i$, $m_B^g = m_A^g(1+\eta)$, where $\eta \neq 0$ is the Eötvös parameter. The figure is not to scale.The deflection angle of the plumb line is very small. Taken from [5].

The violation signal of a torsion balance experiment occurs at zero frequency, which is a difficulty. To avoid this problem, in the mid-1960s Dicke and collaborators used the Sun as source body of a possible violation and therefore exchanged the position of the two masses. Their experiment compared the gravitational and inertial mass of the test bodies which enter, respectively, in the gravitational force from the Sun and in the centrifugal force along the orbit around it. In 1972 Dicke's group reached a precision of 10^{-11}, which was a few years later improved by Braginsky (in Moscow) to 10^{-12}, which is four orders of magnitude better than Eötvös had done.

After Dicke's and Braginsky's experiments it was apparent that the challenge was a rotating torsion balance, in order to achieve in the field of the Earth the same precision

demonstrated in the field of the Sun. That leads to the best present test made by the Eöt-Wash group led by Eric Adelberger at the University of Washington in Seattle. As can be seen in [6], the outcome of the experiment was almost 5 orders of magnitude better than the Eötvös' one and the conclusion is

$$\eta_{weak} < (0.3 \pm 1.8) \cdot 10^{-13}.$$

The next step in precise measurement of Eötvös parameter is leaving the Earth's surface and place the torsion balance experiment in space with (almost) zero-g. As the first one, a French satellite called MICROSCOPE (Micro-Satellite à traînée Compenseé pour l'Observation du Principe d'Equivalence) was launched on 25 April 2016. It started collecting the data in December 2016 and the preliminary results have been reported in 2017. The aim of the experiment is to test WEP to 10^{-15} [7].

The next experiment under study is an Italian non-cryogenic satellite named Galileo Galilei (GG). It should be flown in low Earth orbit as MICROSCOPE, aims at testing the weak equivalence principle to 10^{-17} at room temperature. More details can be seen in [8].

1.1.2 EP for antimatter

There have not yet been any direct measurements including free-fall or gravitational balance, tests of the gravitational interactions of observable matter and antimatter. Moreover, direct gravitational experiments with non-neutral antimatter (isolated positrons or antiprotons) are exceedingly difficult because the electrical forces overwhelm the gravitational forces. As mentioned above, employing neutral antihydrogen or positronium eliminates this complication.

The first rough measurement was reported by a part of the collaboration ALPHA, which is called ALPHA-g (AD, CERN) in 2013 [9]. Their novel method yields directly measured limits on the ratio of the gravitational to inertial mass of antimatter, measured on 434 trapped antihydrogen atoms in ALPHA's octupole magnetic trap. The result set statistical bound on the value of

$$F = \frac{m_g}{m_i}, \tag{1.4}$$

where m_g is the gravitational mass and m_i is the inertial mass of antihydrogen.

Using the method of comparing the positions of actual and simulated annihilation events, they ruled out ratios above $F = 75$ (statistics alone) and $F = 110$ (including worst-case systematic effects) for gravity, and below $F = -65$ (combined systematic and

statistical effects) for antigravity, at the 5% significance level. Unfortunately, this is far away from the result $F = 1$, where small deviations of WEP can be tested. However, ALPHA plans to continue in using this method which can lead to improvement of the measurement.

Chapter 2

The AEgIS Experiment

The AEgIS experiment belongs to the six currently working experiments in the Antiproton Decelerator (AD) hall at CERN (together with ALPHA, ASACUSA, ATRAP, BASE and GBAR). The location of all these experiments is in the zone inside the ring of the Antiproton Decelerator. In this chapter, a quick overview, a hardware schematics of this experiment will be shown and also the detection system used for particle diagnostics together with positron apparatus and the inner trap system of the experiment will be described.

2.1 Antiproton Decelerator

The Antiproton Decelerator (AD) facility at CERN, the only source of cold antiprotons in the world, began operation in 1999. It is an oval-shape synchrotron with the circumference of 188 meters (Figure 2.1). It consists of four straight sectors, where the instruments for cooling of the beam, the RF cavities and diagnostics equipment are placed. For the bending of the beam a series of dipole and quadrupole magnets are used.

2.1.1 Production of antiprotons

The antiprotons are produced by colliding a proton beam on an Iridium target. In a small fraction of collisions, the following reactions occur:

$$\mathrm{p(beam)} + \mathrm{p(target)} \;\rightarrow\; \mathrm{p} + \mathrm{p} + \mathrm{p} + \bar{\mathrm{p}}, \tag{2.1}$$

$$\mathrm{p(beam)} + \mathrm{n(target)} \;\rightarrow\; \mathrm{p} + \mathrm{n} + \mathrm{p} + \bar{\mathrm{p}}, \tag{2.2}$$

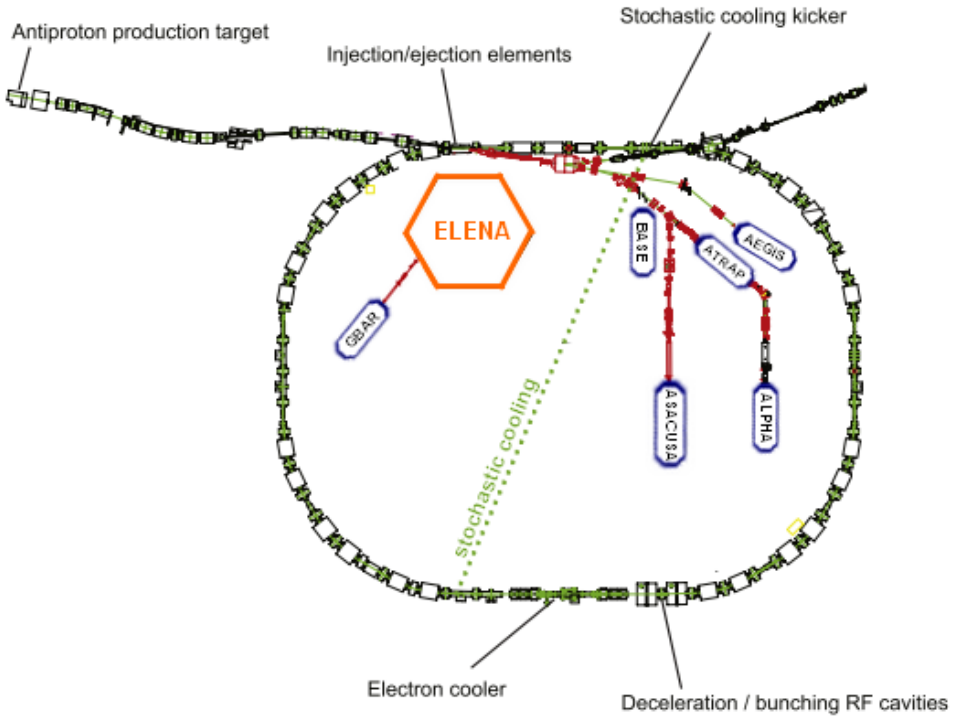

Figure 2.1: Schematics of Antiproton Decelerator, ELENA facility and the position of current experiments. Also, the exact places where the cooling (electron and stochastic) takes place are shown.

under the conservation requirements of energy, momentum, and nucleon number. The schematics of the principle of the production is shown in Figure 2.2.

The minimum kinetic energy required for this reaction is E $\sim$ 6 GeV with laboratory energies of produced $\bar{p}$ and three p $E_{lab} \sim 1$ GeV. In order to increase the production yield, protons with high energies (26 GeV) from CERN's Proton Synchrotron (PS) are used. This corresponds to an energy of produced $\bar{p}$ $E_{\bar{p}} \sim 3.6$ GeV.

During the AD cooling process, this energy is reduced by three orders of magnitude to 5.3 MeV.

2.1.2 AD cooling process

The Antiproton Decelerator cools antiprotons in a cycle with a duration of $\sim$ 120 s, which can be seen in Figure 2.3. It took place in four steps (injection, RF stretching, double stochastic and electron cooling). Places, where all these steps take place can be seen in Figure 2.1.

At first, a beam containing about $1.5 \cdot 10^{13}$ protons produces about $5 \cdot 10^{7}$ (fast) antiprotons, which are injected in the AD (the first region in Figure 2.3).

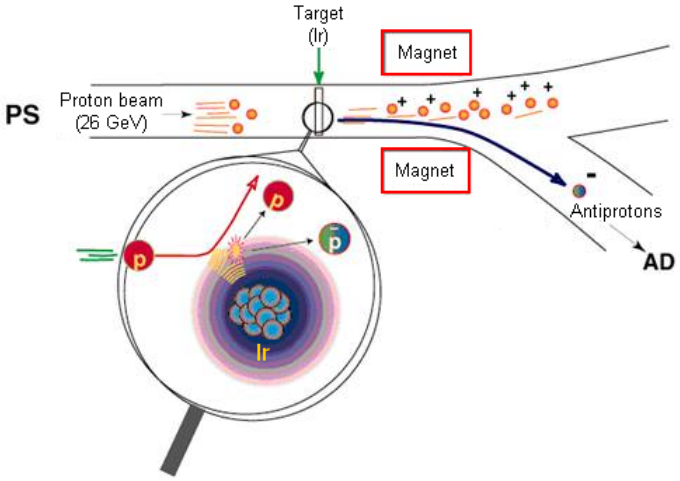

Figure 2.2: Principle of antiproton production. A proton beam collides on an Ir target and a small fraction follows the reaction (2.1) or (2.2) and produce antiprotons, which are then lead to the AD by a magnetic line.

Then, RF fields stretch the pulse lengths from L = 30 m (corresponding to Δ t = 25 ns) to 190 m (Δ t = 150 ns)).

Next, stochastic cooling is applied (first two flat region in Fig. 2.3): special electrodes (Stochastic cooling kicker) are located along the AD in order to detect deviations Δp_i (the momenta) and Δx_i (the transverse position) of small subgroups of $\bar{p}$ relative to the mean values of all $\bar{p}$. These signals are then used for a correction of the subgroups by applying electric pulses from steering electrodes (located on the opposite side of the AD). These pulses are repeated in order to converge the beam and decelerate it to p = 2 GeV/c.

After that, electron cooling of the beam is applied (third and fourth flat regions in Fig. 2.3): at over a 2 m long linear region by an electron beam. Antiprotons loose their energy via Coulomb collisions with e^- and therefore achieve the final momentum of p = 5.3 MeV.

At the end of the cycle, a 100-200 ns long beam, which contains about $3{\cdot}10^7$ antiprotons is extracted into one from five experimental zones inside the AD hall.

2.2 Layout of the experiment

The primary scientific goal of the experiment is to directly measure the Earth's local gravitational acceleration g on $\bar{H}$ with 1% relative precision. The current aim of AEgIS is to form a cold antihydrogen beam at 100 mK.

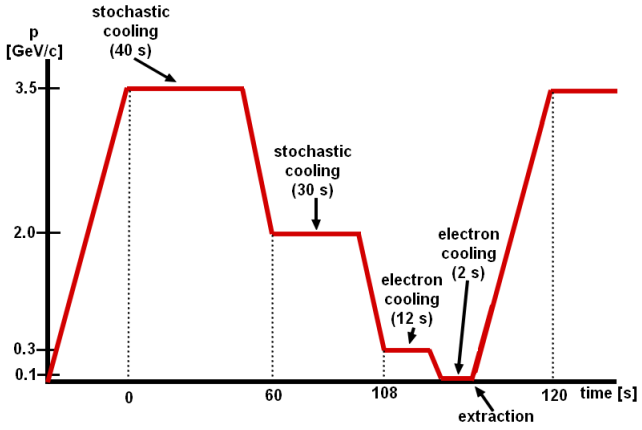

Figure 2.3: AD cooling cycle. The regions, where two types (stochastic and electron) cooling are applied, are shown.

The experiment itself works in several steps as can be seen in Figure 2.4. The advantage of the experiment is that the positron and the antiproton system could work independently to each other.

At first, positrons are produced by a ^{22}Na source, whereupon they are cooled down, captured and accumulated. From the hardware point of view, the positron apparatus is located on the second floor of the experiment as can be seen in Figure 2.5.

The next step is the production of positronium (Ps). The Ps formation mechanism chosen by AEgIS uses a silica converter where positrons are implanted at about keV energy in the surface. The last part concerning positronium is its laser excitation to a high Rydberg state by a group of lasers whose wavelengths are tuned in the range 204-206 nm for the first step ($n = 3$), and 1680-1715 nm for the second step ($n = 15 - 17$).

After that, antihydrogen is finally pulsed-formed by resonant charge exchange between Rydberg Ps and cold antiprotons:

$$Ps^* + \bar{p} \rightarrow \bar{H}^* + e^-. \tag{2.3}$$

This step is the last one in the current experimental setup.

The hardware schematics of the AEgIS apparatus can be seen in Figure 2.5. The positron system is located on the second floor of the set-up, just above the AD antiproton line.

In the first floor the main vacuum chamber is located, connected to the positron system by a positron transfer line. The main apparatus consists of two Penning-Malmberg traps with two sizes of magnetic field generated by a superconducting Niobium Titanium alloy: 4.46 T (originally designed to operate at 5 T), which is used for storing and cooling

antiprotons, and 1 T, which is used for $\bar{H}$ production. The superconducting state is reached by using liquid nitrogen and liquid helium in order to cool the magnets. The external surface is at nitrogen temperature, 77 K, whereas the internal tube (with traps) is at 4 K. The scheme of the magnetic field in the main apparatus is shown in Figure 2.6.

Each region will be described in the next sections.

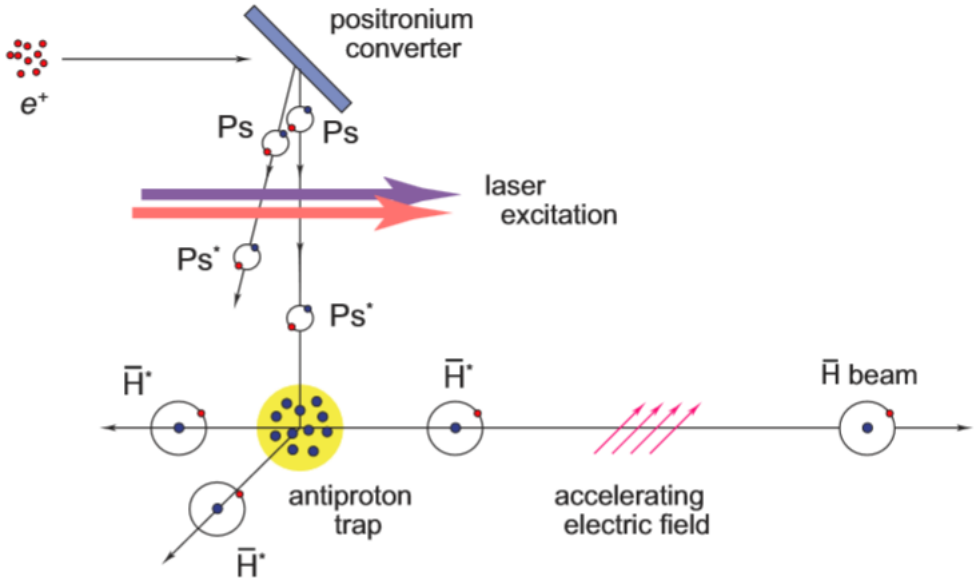

Figure 2.4: A brief scheme of the steps of the experiment. Antihydrogen is produced by a charge exchange of positronium, which is excited by the set of two lasers, and antiprotons, which are stored in the antiproton trap. Taken from [10].

2.3 Detection system and particle diagnostics

AEgIS contains many variable types of detectors in order to diagnose the most important particles - electrons, antiprotons, positrons and antihydrogen.

Moving from left to right in Figure 2.5, the first important detector is 5T micro-channel plate (5TMCP), a 200 MCP in chevron configuration with a P67 phosphor screen and metallized surface. This MCP is able to image the entire full radius of the traps and is placed in the 5 T trap.

In a central region of the experiment, two Faraday cups (FCs) are placed to measure the number of charged particles. FC is the most simple and the most frequent type of charged particle detector. Charged particles enter the cup and hit the collector. Then, secondary electrons are emitted from the collector and the signal is digitized by the readout circuit.

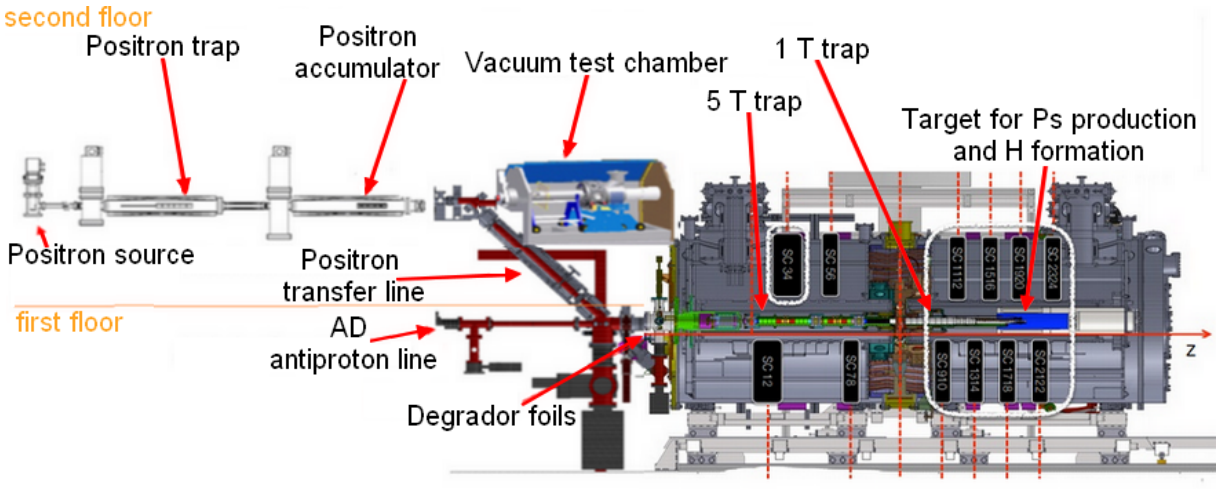

Figure 2.5: Schematic of the AEgIS apparatus. Positron apparatus, antiproton line from AD and the main trap apparatus is shown.

The main detector designed for antihydrogen formation, found around the production trap, is called FACT (The Fast Annihilation Cryogenic Tracking detector). It is the only detector with vertex reconstruction capabilities, composed of 800 z-stacked rings of scintillating fibres arranged in four concentric layers around the production trap with an active region of about 300 mm in length. Each scintillating fibre is coupled to a plain fibre that carries the scintillation light to the external flange of the experiment, where it is read by a Multi-Pixel Photon Counter (MPPC) detector at room temperature. More details about this detector can be seen in [11]

At the end of the apparatus, the field ionization detector MCP (1TMCP) is found. The 1TMCP consists of a 10 MCP assembly in chevron configuration with a P67 fast phosphor screen on the back. This kind of detector can image all charged particles plasmas (electrons, positrons, antiprotons) with a very good definition and stability. Due to this fact it is used as the crucial piece of all diagnostics. An example of the images obtained by dumping different kinds of charged particles is shown in Figure 2.7.

Around the main apparatus of the experiment external annihilation detectors are placed. Firstly, 12 external plastic scintillator slabs are installed around the external surface of the vacuum chamber to monitor annihilations. All scintillators can be seen in Figure 2.5. Each scintillating slab is a cylindrical segment, about 100 mm in width, 20 mm in depth and made of plastic polystyrene doped with POPOP wavelength shifter. It covers a solid angle of about 3 % with respect to an annihilation happening in its centre. Each slab is optically coupled to two heavily shielded coincident photomultiplier tubes (PMTs).

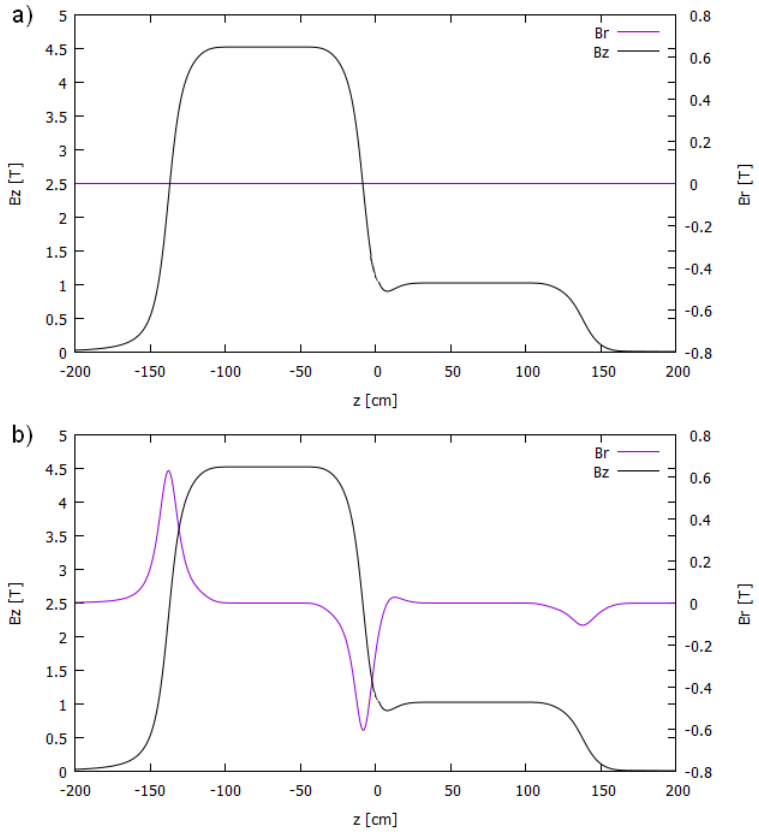

Figure 2.6: Magnetic field in the AEgIS apparatus. a) on-axis field; b) 5 cm off-axis field. Both field are shown: parallel to the axis (B_z) and transverse to the axis (B_r).

Secondly, 2 CsI crystal scintillators are placed in the apparatus to determine the number and possible losses of positrons during the accumulation and transfer.

This list of detectors names only the most important and main ones in the apparatus. For further diagnostics many secondary detectors are used in the experiment.

2.4 Future of the experiment

After the planned shut-down in 2019-2020, new antiproton decelerator called ELENA (Extra Low Energy Antiproton Ring) will be connected to the AD. ELENA plans to use double electron cooling of antiprotons which means decelerating the particles from momentum of 100 MeV/c (5.3 MeV in energy) down to 13.7 MeV/c, which corresponds to kinetic energy of 100 keV [12].

However, the main motivation for building ELENA is to significantly increase the number of antiprotons usable for physics due to degrading the energy and therefore no need of usage of degrader foils (and loosing antiprotons) in the experiments.

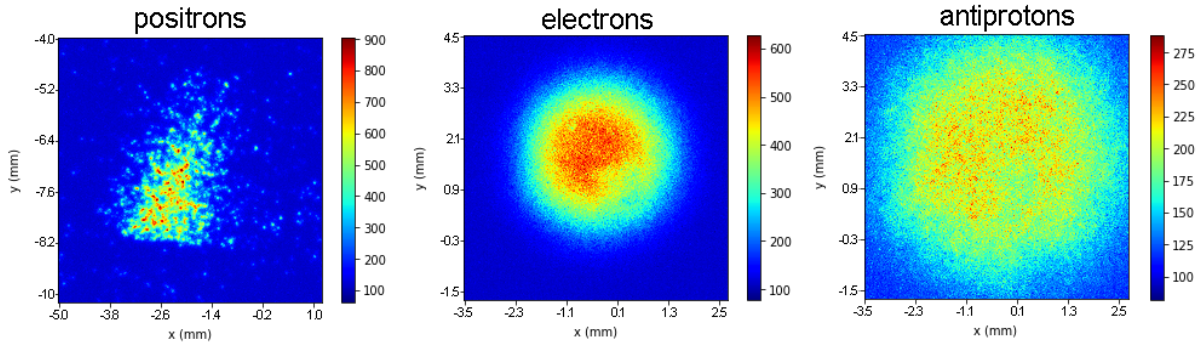

Figure 2.7: An example of MCP image of positrons, electrons and antiprotons.

Another advantage of ELENA should be the availability of the beam due to its serving up to all experiments simultaneously, which will give users much more beam time.

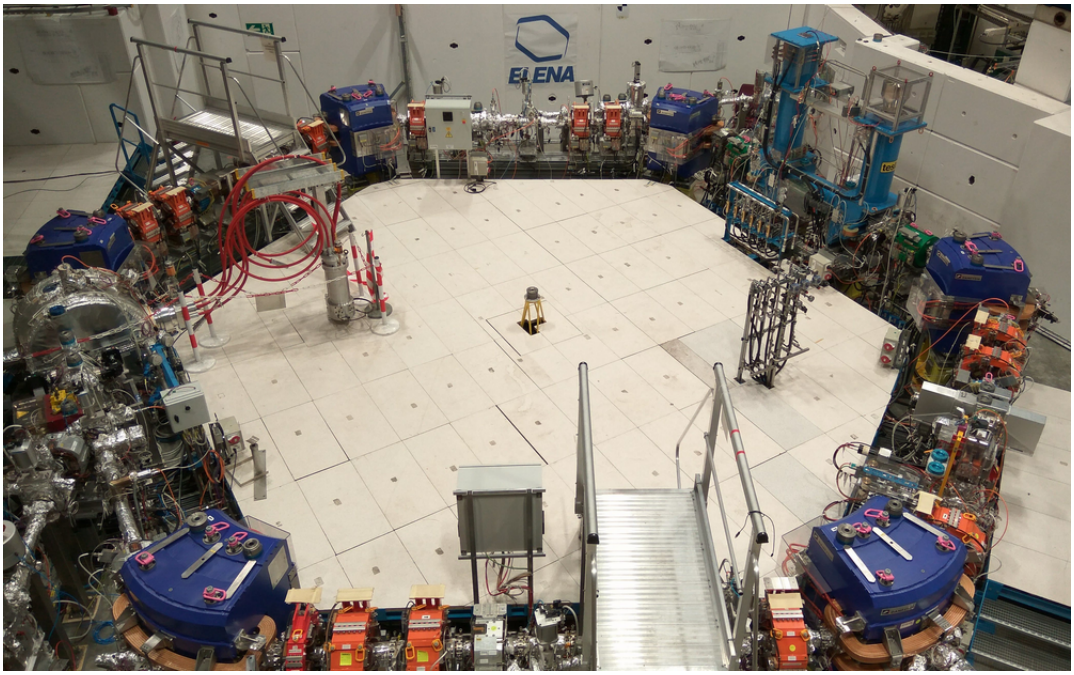

Figure 2.8: The photo of the decelerator ELENA (taken in August 2018).

2.5 Positron and positronium system of AEgIS

The formation of cold positronium atoms is one of the key conditions which need to be fulfilled for a successful antihydrogen formation. In the first part of this section, the positron apparatus of the experiment will be described and the positronium formation and excitation will be shown in the second part.

2.5.1 Positron system

The main positron system of the experiment is schemed in Figure 2.9 and contains mainly three elements: a positron source (with a moderator), a cooling trap and an accumulator for storage. After that the system is divided into two parts: one leads to the main apparatus and the second one via electrostatic buncher to the target chamber, where measurement at room temperature can be done.

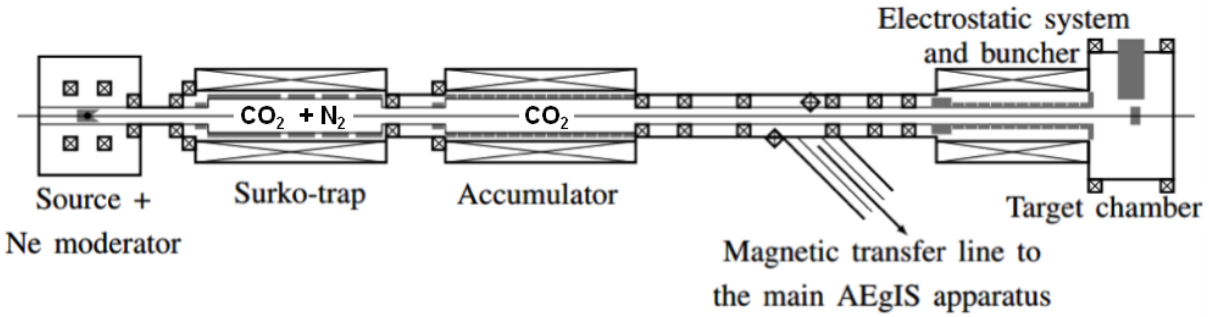

Figure 2.9: Scheme of the AEgIS positron system. Positrons leave the source, then are moderated by liquid Ne, cooled in the Surko trap and stored in the accumulator. Magnetic lines then carry particles to the main apparatus or to the target chamber.

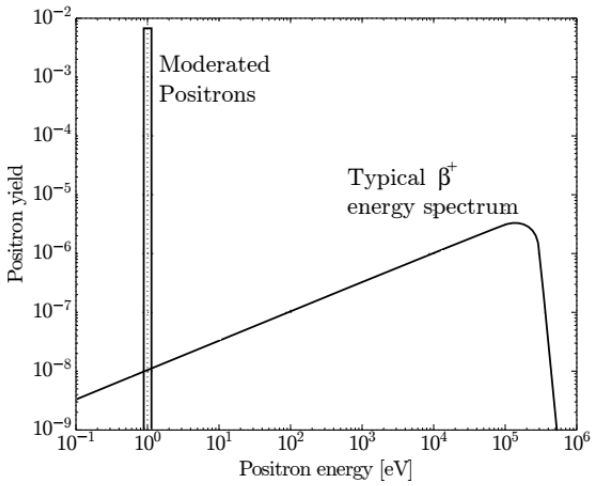

Figure 2.10: A typical energy spectrum of β^+ decay compared with the energy of moderated positrons.

2.5.1.1 Positron source and moderator

Positrons are emitted by a β^+ decay of a ^{22}Na radioactive source with a half-life 2.6 years. In March 2012, a 21 mCi radioactive source was placed at the beginning of the positrons

apparatus. In 2015, the radioactive source efficiency decreased to 11 mCi, so in the year 2016 a new source, 50 mCi, was installed. This replacement provides about four times more positrons than before.

Due to the fact that positrons are emitted in a wide range of energies (see Figure 2.10), a moderator, which cools them down is needed. The moderator chosen by AEgIS consists of a thin solid film of Neon deposited directly on the surface of the source and its holder. For growing it, a Ne gas is injected into the source chamber, and freezes on the source holder, set at 7 K via a closed Liquid Helium. The energy of moderated positrons is cooled down to a few eV (moderated positrons can be seen in Figure 2.10).

2.5.1.2 The Surko trap

The slow positrons are then extracted into the so-called Surko trap. The Surko trap is a special Penning-Malmberg type trap, which uses a buffer gas to cool down the positrons (more information about the Penning-Malmberg traps is provided in the section 2.6). The principle of the trap is simple: particles lose the energy by inelastic collision (which are much more probable than annihilations) with the molecules of gas inside the trap.

The Surko trap which is used in AEgIS has three stages, each with a lower potential (and also lower gas pressure) than the one before (can be seen in Figure 2.11). In this kind of trap, N_2 (in the first two stages) and CO_2 (in the third stage) are used as the buffer gasses.

In the first stage, the cooling of positrons needs to be very effective and that leads to a need of high pressure of the gas ($\simeq 10^{-4}$ mbar). Consequently, the lifetime of positrons is lowered to a few milliseconds.

Cooled positrons are then loaded into the second stage. This stage has a lower potential than the previous one, so positrons cannot escape and they get colder.

After that, positrons fall into the third potential well, where they are cooled down by the mixture of N_2 and CO_2. To compress the positron plasma, a Rotating Wall (RW) is applied in the third stage. The RW technique applies a rotating electric field in order to couple it with the plasma to inject angular momentum. CO_2 is used for the compensation of heating by applying RW technique.

The three stages of potentials are shaped with 6 electrodes and the magnetic radial confinement is done with a 0.07 T magnetic field.

The positrons are released from the trap every 0.15 seconds with energy of about 17 eV. The number of positrons in each bunch has been measured by a set of CsI detectors and

be estimated to $(2.7 \pm 0.3) \cdot 10^4$. The efficiency of the trap (the ratio between injected and released positrons) was measured to be $\eta_{Surko} = 1.4 \cdot 10^{-1}$ [13].

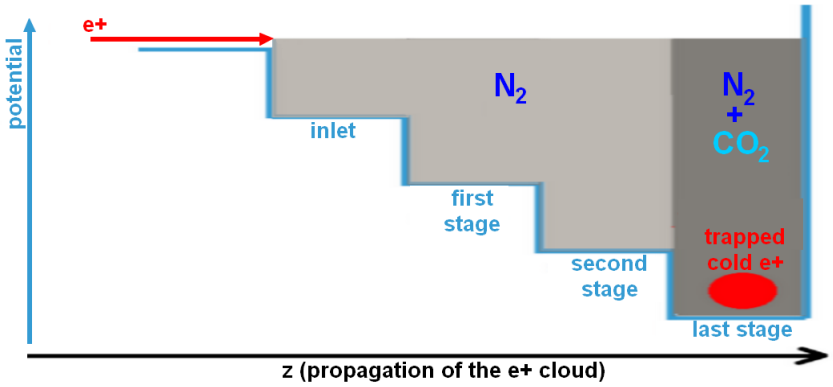

Figure 2.11: The potential in the three-staged Surko trap used in the AEgIS experiment. Emitted positrons enter by the inlet electrode, collide with buffer gas and get cooled. Finally they are accumulated in the last stage, where rotating wall (RW) compression is applied to them.

2.5.1.3 The accumulator

Positrons which are extracted from the Surko trap are magnetically transported into the positron accumulator. This accumulator is also a Penning-Malmberg trap and it uses CO_2 to compensate the heating from RW, which compress positrons.

In comparison to the Surko trap, the accumulator has much lower pressure ($6 \cdot 10^{-8}$ mbar) and the magnetic field used for the radial confinement is higher, 0.1 T. The longitudinal confinement is ensured by a harmonic potential about 14 V deep. Due to these properties, the lifetime of positrons is increased to minutes and that allows to store pulses from the Surko trap.

The trap itself consists of 23 electrodes with the inner radius of 1.27 cm, which makes the harmonic potential well. The first, inlet electrode, can be moved up and down and therefore allows the positrons to come in the accumulator, but not escape. Using this movement, the trap can be filled several times with positrons stacked inside. The maximum storage time is $\simeq 9$ minutes.

The number of positrons stacked in the accumulator was measured by opening the trap after given pulses and counting the number of positrons from the number of annihilations on a target. With the old source (11 mCi), up to 5000 pulses can be stored. The number of stored positrons versus the number of pulses can be seen in Figure 2.12.

The ejection of the positrons is performed by changing the shape of potential from harmonic to the linear (as can be seen in Figure 2.13) and the energy of positrons have to be increased up to 500 eV so they can be transferred to the main apparatus without being back-reflected by the 5 T magnet.

If the positrons are not transferred into the main apparatus, but into the target chamber, the energy of 100 eV is enough to succeed.

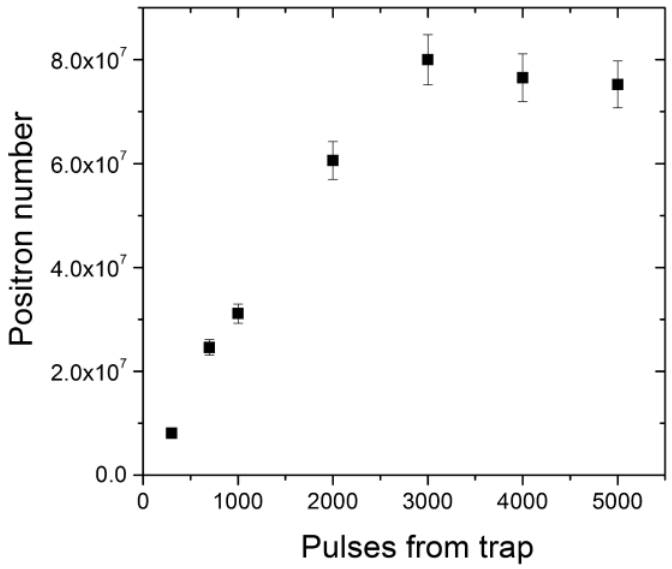

Figure 2.12: The number of stored positrons versus the pulses from Surko trap for the intensity of the radioactive source 11 mCi. Taken from [14].

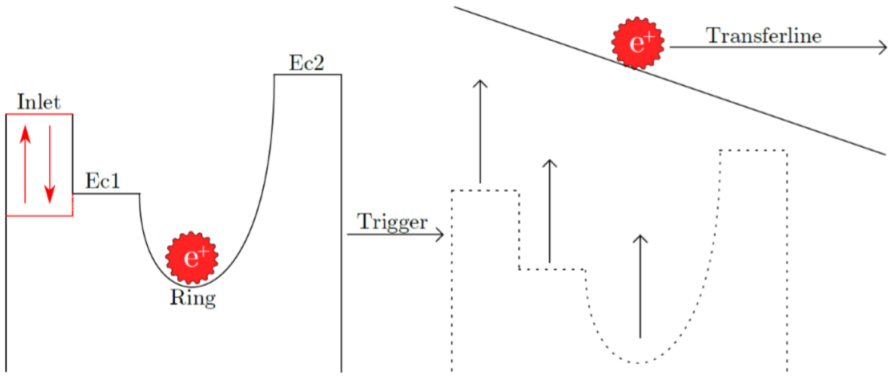

Figure 2.13: Scheme of the potential inside the positron accumulator. Left: harmonic-shaped potential, which allows to store positrons (and inlet electrode, which allows the positrons to enter). Right: changing the potential to a linear shape in order to increase the energy of positrons and ejecting them from the accumulator.

2.5.1.4 The target chamber

In order to study positron and positronium physics, a test target chamber was built at the same level as the whole positron system.

The target chamber operates at the room temperature and the magnetic field is tunable from less than 2 Gauss to 300 Gauss to provide various measurements. The non-presence of a magnetic field is convenient for spectroscopic measurements, for instance.

In order to inject the positrons from the accumulator into the chamber, a transfer line called a buncher was built. The buncher with the target chamber can be seen in Figure 2.14.

The buncher itself consists of 25 electrodes which generate an electric field needed for the transport, which means that no magnetic field is needed in this stage. Three more electrodes are needed for decreasing the magnetic field at the beginning and for the spatial focus. The main aims of the buncher are following:

1. Extract positrons from the magnetic field of the accumulator and drive them towards the target chamber

2. Accelerate positrons to the required energy to implant at a depth in the converting material that allows efficient thermalization

3. Spatially focus the positron cloud on the target

Every electrode in the buncher is 1.6 cm long, that means that the buncher has a length of 40 cm. Consider the fact that the bunch of positrons is $\simeq$ 20 cm long, there is no problem in containing the whole pulse between the first and the last electrode. They then form two lenses, so the e^+ bunch is focused in the middle of the buncher (as can be seen in Figure 2.14).

When the positron pulse arrives, a parabolic potential is raised between the first and the last electrode in order to compress the pulse in time (from 20 - 30 ns to about 7 ns) and space (few mm, depending on the electromagnetic conditions). It also allows to accelerate the bunch, from energy of 100 eV to the required implantation energy, typically 3.5 keV (up to 7 keV).

In Figure 2.15 (left) the image of the compression of pulses at the MCP can be seen. On the right, we can see two annihilation curves. The energy of positrons during this measurement was 3.3 keV and the magnetic field was below 1.8 G. One is obtained without the buncher and the FWHM for this curve was 21 ns. On the other side, with buncher on the FWHM was 7 ns.

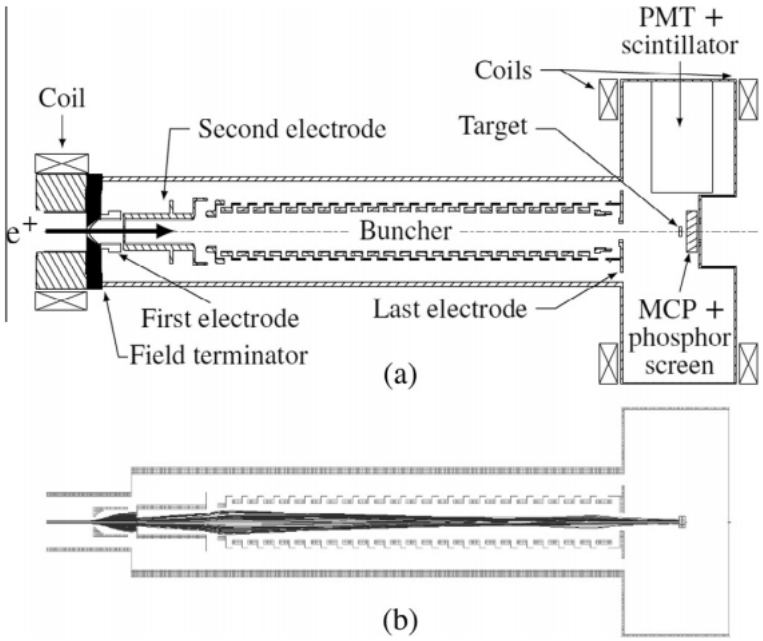

Figure 2.14: (a): Sketch of the electrostatic system. (b): Simulation of positron bunching and focusing from the end of magnetic section to the target. Taken from [14].

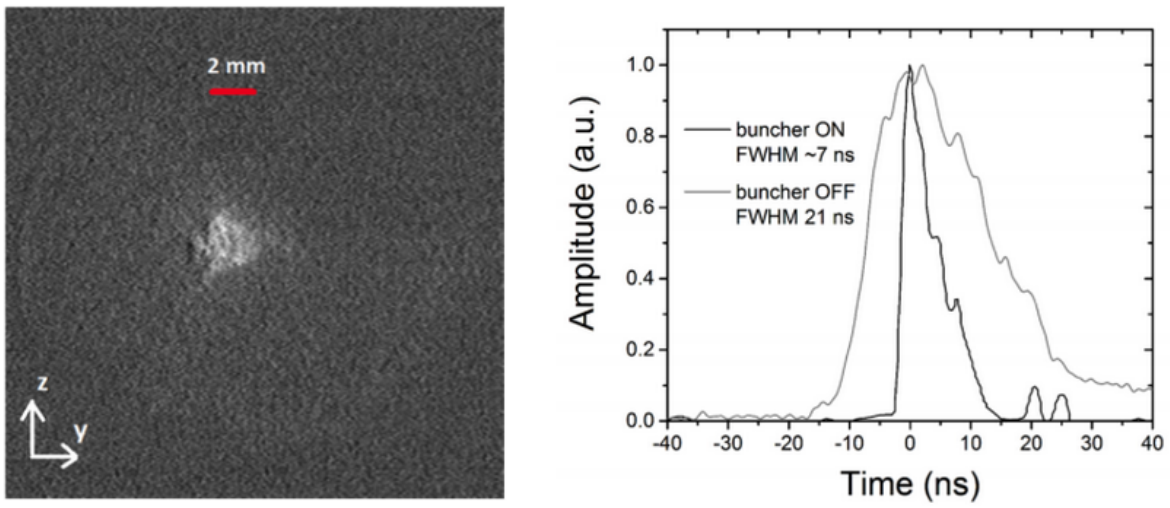

Figure 2.15: Left: positron image at the MCP. Right: Comparison of the two annihilation curves obtained with and without the electrostatic buncher, showing bunching and time-focusing of the positron cloud on the target (the HV puls was set to 4200 V). Both signal are normalised to the same amplitude. Taken from [15].

2.5.2 Positronium

Positronium (Ps) is a bound state of an electron (e^-) with its antiparticle, a positron (e^+) with the binding energy of 6.8 eV. It is the lightest known atom, experimentally discovered in 1951.

As Ps binds one particle and its antiparticle together, it has a short life-time and other interesting properties.

Depending on the configuration of spins of electron and positron, Ps has two ground states. The singlet state with anti-parallel spins (and a total spin equal to zero) is called para-positronium (p-Ps), its life-time is around 125 ps and it annihilates in 2γ (with the energy of 511 keV each) emission.

The triplet state with parallel spins (and a total spin equal to one) is called ortho-positronium (o-Ps). The lifetime of o-Ps is 142 ns in a vacuum (15 ns in a magnetic field of 1 T) and it annihilates in 3γ (with a total energy of 1022 keV).

2.5.2.1 Positronium production

The positronium is usually produced by a beam of positrons (with an energy 50 eV to 15 keV) injected into a porous material. When a positron is implanted into a thin film, it will scatter off atoms and electrons in the solid and slow to atomic-scale energy (several eV) very quickly. The behaviour of the positrons in porous materials can be seen in Figure 2.16.

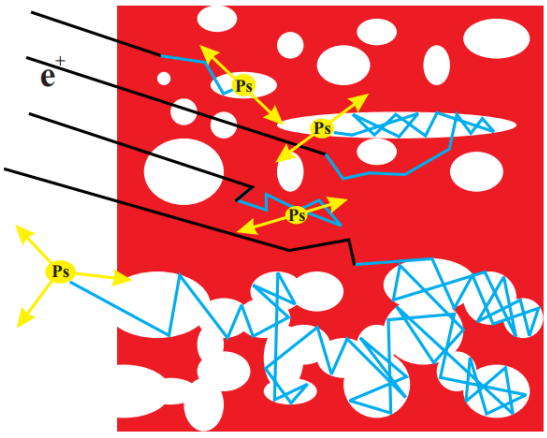

Figure 2.16: The production of positronium in a porous material. Taken from [17].

As a target for Ps formation in experiment AEgIS, a silica-based target is used. Inside the target, nano-channels (of about 5-15 nm diameter) are formed and its surface is

oxidized to form a thin layer of silica. This kind of target was chosen because of the following reasons:

1. In silicon, positrons have a long diffusion length before annihilation, which allows positrons to release energy and therefore form Ps, which is emitted into the nano-channels.

2. The target is able to be operated at very low temperatures (nominally 100 mK).

3. This kind of target has the highest efficiency in producing Ps in the material bulk at low temperatures (about 50 %).

The Ps formation and emittance can be controlled by so-called single-shot positron annihilation lifetime spectroscopy (SSPALS). It is based on detecting the γ-rays from the annihilation of Ps. The results from this measurement can be seen in Figure 2.17 (the energy of positrons was 3.3 keV). In the figure the tail, which prove the Ps formation is clearly visible.

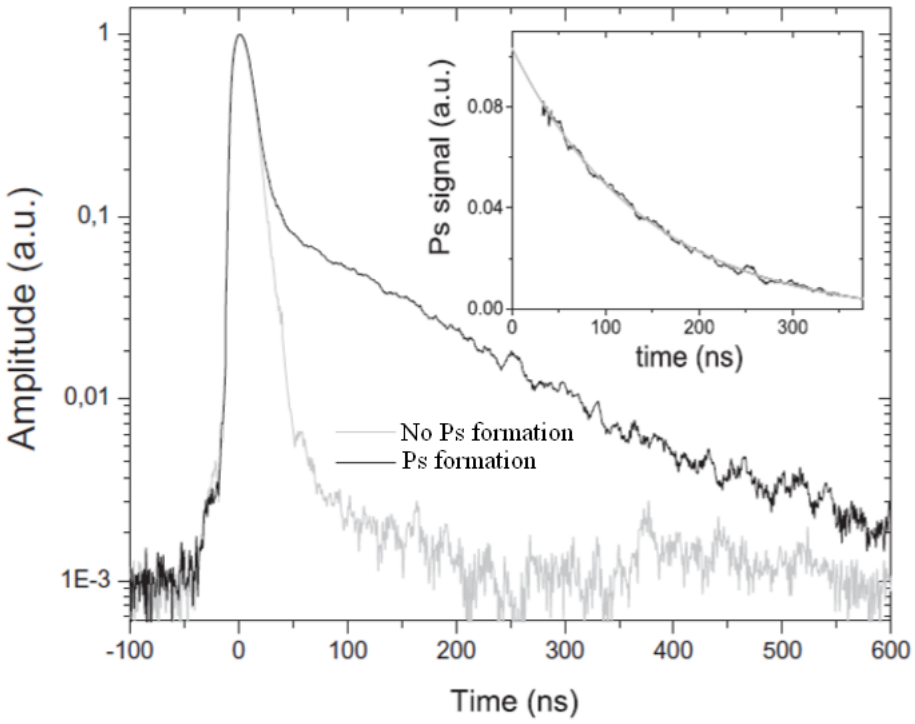

Figure 2.17: SSPALS spectra measured on MCP. Grey line: no Ps production; black line: Ps production. Taken from [15].

2.5.2.2 Positronium excitation

In order to produced the antihydrogen by the reaction (2.3), it needs to be excited to a high Rydberg state. By this excitation, we increase the rate of produced antihydrogen because the cross section of this reaction scales as $\sigma \propto n_{Ps}^4$, where n_{Ps} is the positronium principal quantum number. Moreover, the Ps cloud will be able to achieve the $\bar{p}$ cloud more easily, because the life-time of excited Ps is much longer.

The excitation itself occurs inside the 1 T magnet between the on-axis and off-axis trap. The exact place of excitation can be seen in Figure 2.18, where the photo of the production trap and the target is shown.

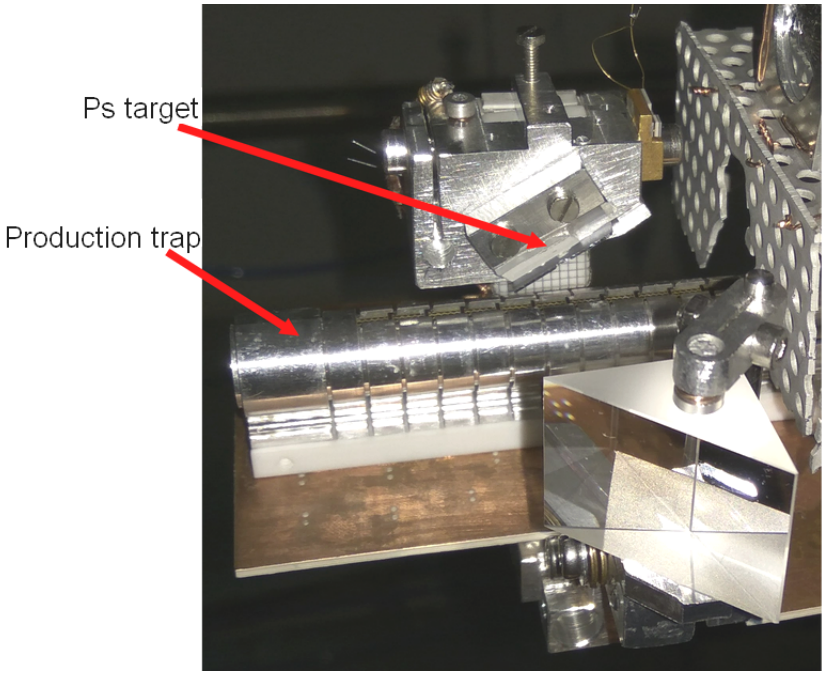

Figure 2.18: The photo of the area, where the excitation takes place.

The excitation takes place in two steps. At first, Ps is excited by an UV laser with a wavelength $\lambda \sim 205$ nm from a 1^3S state to 3^3P state.

Then, Ps is excited from $n = 3$ to $n = 15 - 17$ with an IR laser with a wavelength $\lambda = 1680 - 1715$ nm. Achieved life-time of Ps* is then in order of microseconds, which is enough for reaching the antiproton cloud (placed around 2 cm from the production target).

2.6 AEgIS inner trap system

Trap system is the most important part of the AEgIS experiment. All charged particles (electrons, antiprotons, positrons) are cooled, trapped and manipulated in two cryogenic environments with the magnetic induction of 5 T and 1 T provided by superconducting magnets. In this section, the system of inner traps will be described in its current status.

2.6.1 Penning trap

The ideal Penning trap is based on the superposition of a homogeneous magnetic field (for the radial confinement of the beam) and a static electric potential (for the axial confinement if the beam). The ideal electrostatic potential of such a trap is quadratic:

$$\phi(x, y, z) = \frac{V_0}{2d^2}\left(z^2 - \frac{x^2}{2} - \frac{y^2}{2}\right), \tag{2.4}$$

where x and y are radial components and the magnetic field $\vec{B} = (0, 0, \mathrm{B_z})$ is applied along the z axis. V_0 is the difference between the potential at the first (ring) electrode and the last (end-cap) electrode and d is the characteristic size of the trap, $d^2 = 1/2\,(z_0^2 + r_0^2/2)$, where r_0 and z_0 are the minimum distance between the center and the end-cap (or ring) electrode (depicted in Figure 2.19).

In this type of a trap, the movement of the particles is harmonic and the frequency of axial motion is independent of its energy and can be changed by the potential V_0:

$$\omega_z \equiv \sqrt{\frac{qV_0}{md^2}}, \tag{2.5}$$

q and m is the charge or mass of the trapped particle.

In order to achieve the ideal electrostatic potential, the shape of the electrodes of the trap needs to be hyperbolic, as can be seen in Figure 2.19. However, this shape of the trap has some disadvantages:

1. It is difficult to obtain a hyperbolic shape of the electrode
2. Loading of the particles is performed by making a hole in the center of one end-caps and that perturbs the field lines and therefore the trapping stability
3. Due to the finite size of the hyperbolas, the electric field is not perfectly homogeneous

However, a cylindrically symmetric electrode structure that creates a saddle point also has a harmonic potential of the form of Eq. (2.4) in a small region around its center.

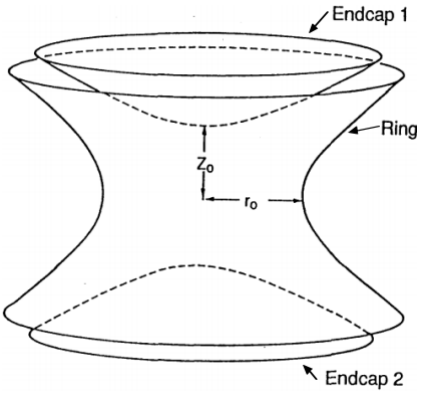

Figure 2.19: The ideal Penning trap geometry - hyperbolic shape. Taken from [18].

Using this fact, the open-ended cylindrical-type Penning trap was studied in details and then widely used. This shape of the trap can be seen in Figure 2.20.

The cylindrical shape of the traps solves the problem with injecting of the particles, since they are injected along the main (magnetic field and electrode) axis.

In the beginning, the structure was similar to the hyperbolic-shaped trap, with the structure of three electrodes (two end-caps and the central one). Later, two so-called 'guard' (or correction) electrode rings were added between the ring and the end-cap, which meant five electrodes in total. However, later studies (with the usage of computing power) showed, that by adding another two correction electrodes, exactly the same harmonicity as in the hyperbolic-shaped trap can be reached.

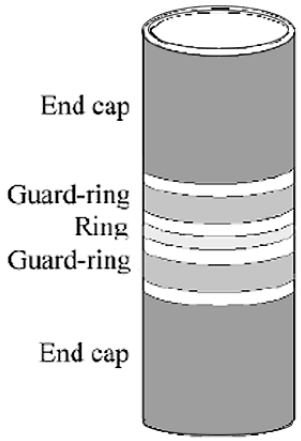

Figure 2.20: The open-ended cylindrical trap. Taken from [19].

2.6.2 Malmberg trap

The next type of a trap for charged particles is a simplified version of Penning trap, so-called Malmberg trap. This trap generates a square-shaped potential (the shape can be seen in Figure 2.21 b)) and is usually used for a confinement of pure electron plasma. The trap itself is composed of a set of cylindrical shaped electrodes and the potential is reached by setting the central electrode to the ground and the other electrodes (end-caps) to the trapping voltage V_c. A simple schematic of the electrodes can be seen in Figure 2.21 a). Usually, the length of the central electrode of the trap is bigger than its inner radius.

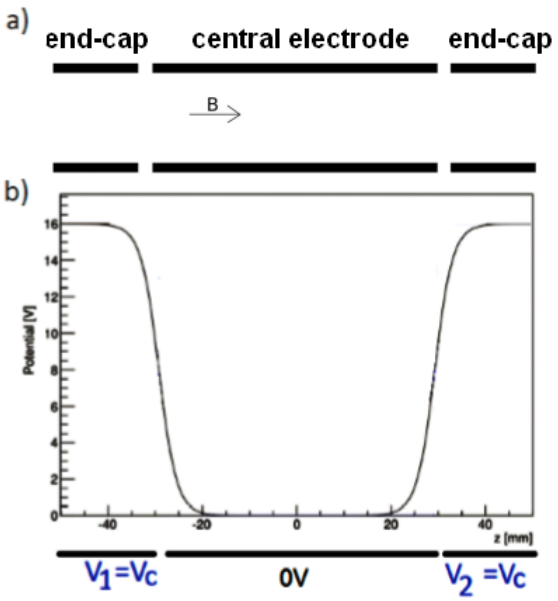

Figure 2.21: Malmberg trap; a) a simple schematic of electrodes; b) a flat potential inside the trap.

Since there is a difference between the potentials, also the motion of particles is different. In a Malmberg trap, the particle doesn't feel any electric field in the region of the central electrode, the only part of the trap, where the electric field can be felt is close to the end-caps. Therefore, particles undergo cyclotron oscillations in the magnetic field and they are confine between the end-caps.

Each of the end-caps can be used as a 'door' to the trap by changing the voltage on it. For loading the charged particles (pbars for instance), the voltage on the first end-cap is lowered to the ground, in order to let the particles enter the trap. When all the particles are in the trap, the voltage is set back to V_c and the particles are trapped inside the

potential well. To eject the particles from the trap, the voltage on the second end-cap can be grounded. This procedure is shown in Figure 2.22.

A trap, which can combine both of the potentials (the harmonic one and the square-shaped one) is called a Penning-Malmberg trap.

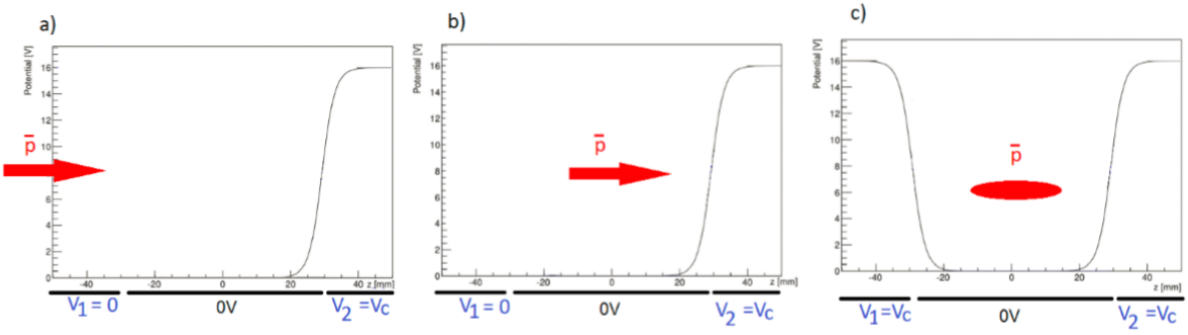

Figure 2.22: Malmberg trap: a) loading of the particles, b) the enter of particles, c) pbars are trapped.

2.6.3 AEgIS trap system

The AEgIS trap system is the most important hardware part of the experiment and it is located in the cryogenic environment of the main experimental apparatus, inside the 4.5 T and 1 T magnets (the experimental apparatus can be seen in Figure 2.5). The aim of the trap system of the experiment is to store, cool and manipulate antiprotons, positrons and formed antihydrogen atoms.

Due to its purpose, the chosen geometry is so-called Multi-Ring Trap one, which means the Penning-Malmberg trap, composed of many short cylindrical electrodes of the same length. With such a configuration, the trap potential can be changed easily just by changing the voltage applied to the trap's electrodes. Using this change, the harmonic potential can be moved along the axis (with shifting the plasma inside) and also a non-harmonic potential can be used.

The system is composed by 102 electrodes, contains 7 traps and is divided into two regions as the magnetic field around them: 4.5 T and 1 T. The schematic of the trap system is shown in Figure 2.23.

2.6.3.1 The 4.5 T Penning-Malmberg trap

This trap is the first part of the apparatus, which is used to manipulate with the antiprotons coming from AD. The length of the trap is around 1 m with inner radius $r_0 = 15$mm.

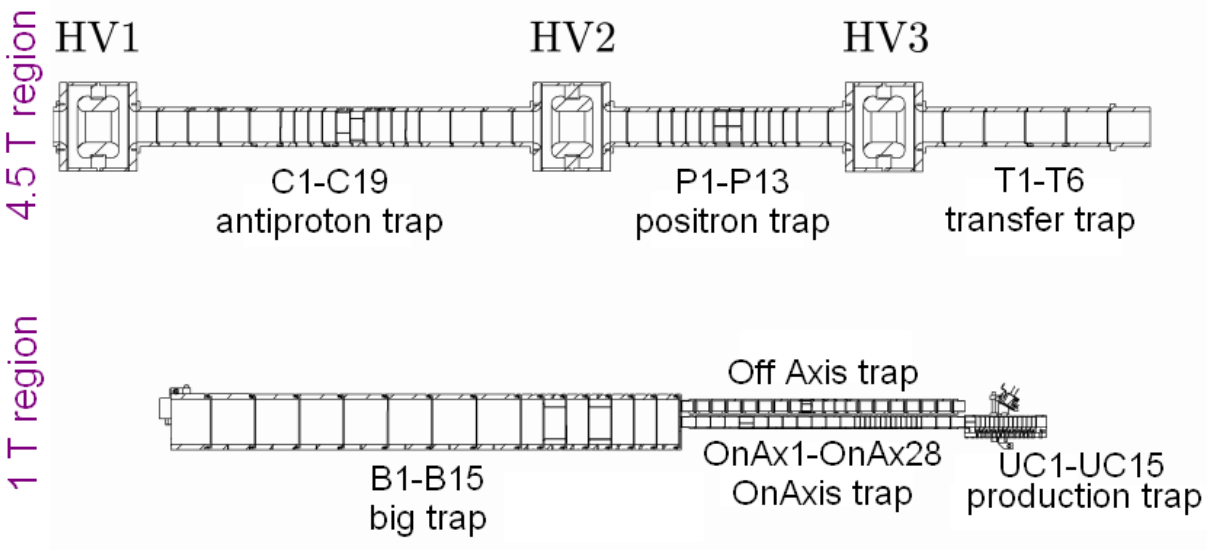

Figure 2.23: The whole trap system of AEgIS inside the main apparatus. The system is divided into two main parts (4.5 T and 1 T region) and it consists of 7 traps and 3 HV electrodes.

The trap itself is divided into two smaller parts, named Catch (C) and Positron (P) (can be seen in Figure 2.23). As the end-caps of these traps, three HV electrodes set to 9 kV are used.

The purpose of this trap is:

1. for antiprotons - catching, electron cooling, accumulating and compression,
2. for positrons - catching, accumulation and compression,
3. transfer to 1 T region.

which is achieved by using three types of electrodes:

1. the standard gold-plated aluminium low voltage ($\pm$ 200V) electrodes, with three types of length (13.5 mm, 30 mm and 40 mm),
2. electrodes for rotating wall compression - gold-plated aluminium split electrodes sectored azimuthally into 4 equivalent sectors 13.5 mm long each,
3. high voltage (max -20 kV) electro-polished Titanium electrodes used as end-caps of the trap. These electrodes are set to 9 kV.

The connection of 4.5 T and 1 T region is provided by a transfer trap, which consists of 6 electrodes. In the center of the transfer section, a movable electrode (B0) is installed, in order to steer the beam. This electrode is placed in the middle of the apparatus, at the position $z = 0$.

2.6.3.2 The 1 T trap

The region of 1 T traps is much more complex than the 4.5 T one. The purpose of this trap is to produce antihydrogen atoms with all the requirements which are necessary for that. The trap system is divided into four regions (see Figure 2.23 and 2.25): The Big trap, the On/Off Axis trap and the Production trap.

The purpose of the first trap, called Big (B), is to catch and compressed antiprotons coming from the 4.5 T region. This trap consists of 15 electrodes with the inner radius $r_0 = 22$ mm. At the beginning of the trap, 8 transfer electrodes with the length of 44 mm are placed. Next 7 electrodes have the length 22 mm and they are divided into 4 azimuthally equal sectors in order to apply the effect of rotating wall to compress antiprotons. At the end of the trap, a flat electrode is used as an end-cap.

The Big trap then split into two smaller traps (with inner radius $r_0 = 5$ mm). One of these traps remains on the main axis and therefore is called the OnAxis trap. The purpose of this trap is the antiproton compression and the transfer to the production trap.

The total length of the OnAxis trap is 28 cm and it consists of 14 transfer electrodes with the length 14 mm, 13 electrodes with the length same as its radius (5 mm) and also one electrode with the length of 14 mm, which is divided into sectors in order to use a rotating wall effect to compress antiproton plasma.

Above this trap, so-called OffAxis trap is placed. This trap was designed as a high-voltage trap in order to raise the energy of positrons before implanting them to the positronium converter. However, the trap was removed in 2016 and now the only purpose is to move positrons to the target.

The OnAxis trap is followed by the final Production (or UltraCold) trap, which is the main (and the most important) part of the experiment. In this place, antiprotons are cooled down and the antihydrogen is produced.

The trap itself is made by 15 electrodes with the inner radius $r_0 = 5$ mm. 13 electrodes have the same length $l = 0.9$ and the radius $r_0 = 4.5$ mm and two electrodes with the length of 10 mm are used as end-caps. Moreover, the first electrode (UC1) is divided into four sectors, so RW can be applied if needed. In that case, the last electrode of the OnAxis trap is used as the end-cap.

All of the 13 central electrodes have small apertures in order to let the Rydberg Ps enter the trap from above. The photo of this trap is shown in Figure 2.24.

The photo of the 1 T region is shown in Figure 2.26.

The summary of all traps used in the experiment is listed in Table 2.1.

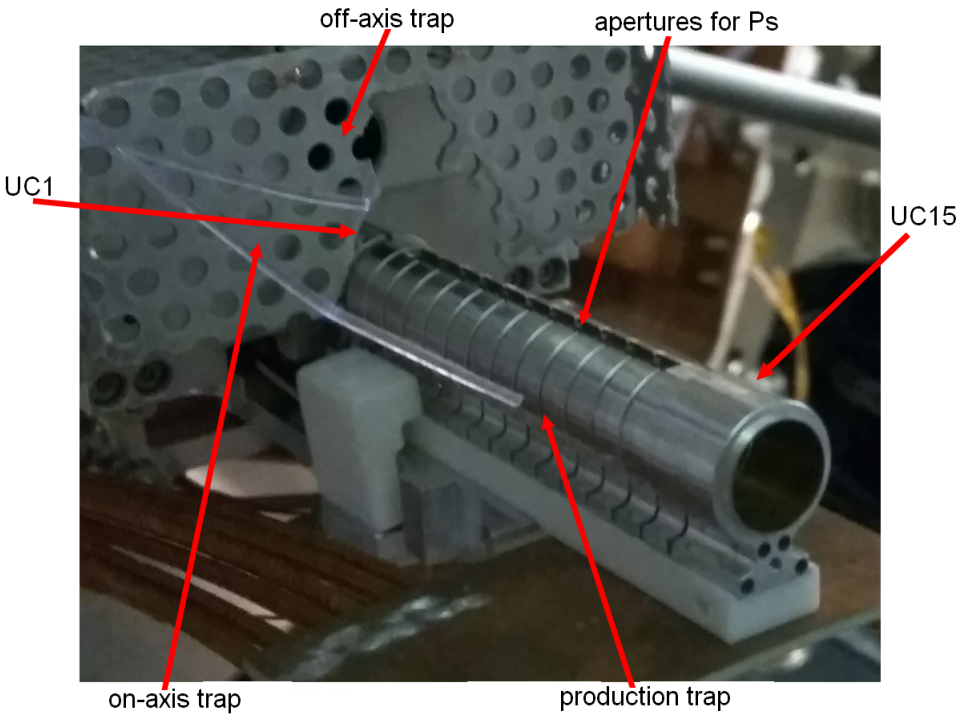

Figure 2.24: The detailed photo of the production trap. The target for Ps formation, which is placed above the middle of the trap (UC8), is not placed.

region	Catch	Positron	Transfer	Big	OnAxis	Production
# electrodes	19	13	6	15	28	15
r [mm]	15	15	15	22	5	5
l [mm]	400	240	230	506	280	78

Table 2.1: Summary of all the traps in the AEgIS experimental system. B0 and HV1,2,3 were omitted.

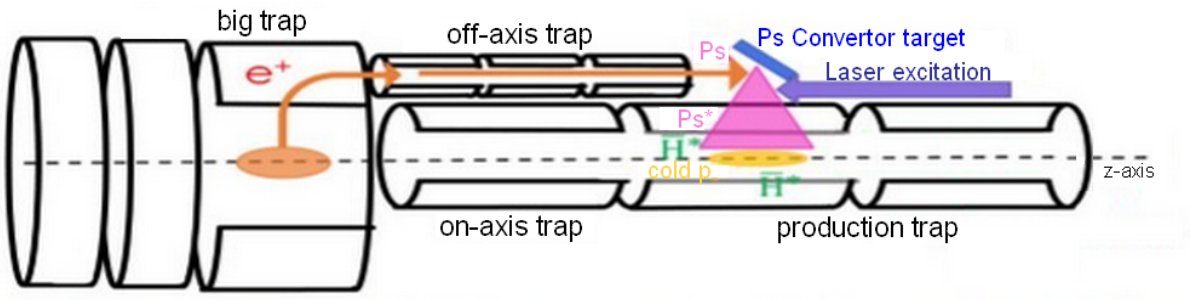

Figure 2.25: The region of the 1 T magnet. The end of the Big trap, the division into two smaller (OnAxis and OffAxis) traps and the Production trap can be seen. The mechanism of the antihydrogen production is shown - the purple triangle stands for incoming Ps*.

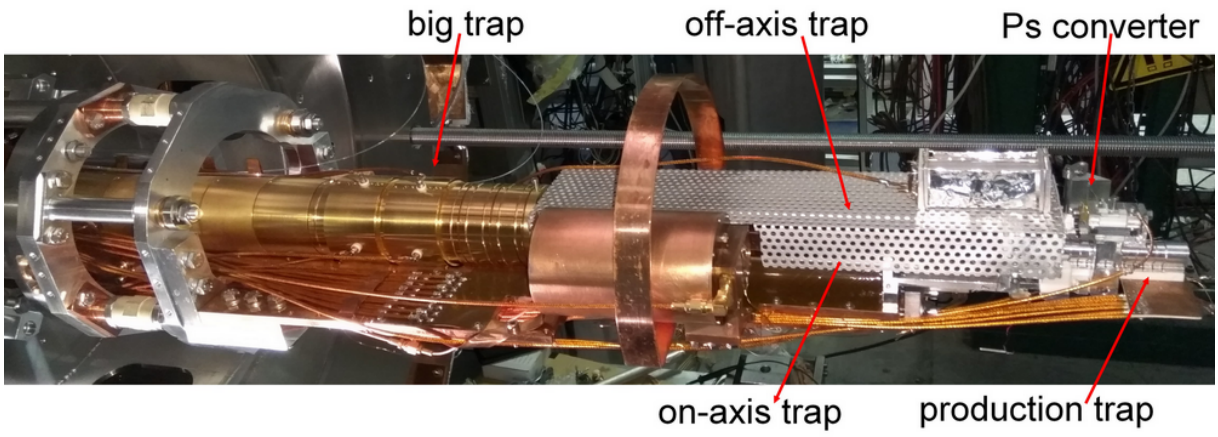

Figure 2.26: Photo of the 1 T region. The Big trap, the Ps converter and the Production trap can be seen, the on-axis and off-axis traps are covered with a shielding.

Chapter 3

Antihydrogen Production

Most of the operation of AEgIS during the year 2018 was dedicated to the antihydrogen production. In this chapter, different ways of production will be discussed with the focus to the three-body charged recombination one, chosen by AEgIS.

3.1 Production of fast antihydrogen

Since the discovery of the antiproton, it was well-known how to produce antiprotons and positrons, but they always moved at almost the speed of light. The formation of antihydrogen then can undergo only at low relative velocities.

In 1983, the world's first low-energy antiproton ring (LEAR) was commissioned, with receiving up to 6% of CERN's formed antiprotons and provided intensity up to 10^{10} $\bar{\mathrm{p}}$ in the 0.1-2.0 GeV/c momentum range.

In 1995, LEAR hosted the first experiment ever to produce antihydrogen atoms. The idea of the formation was simple: when an antiproton passes through the Coulomb field of a nucleus with charge Z, it creates an e^+e^- pair. Then, the antiproton can capture a positron from this produced pair and form antihydrogen:

$$\bar{\mathrm{p}} + Z \rightarrow \bar{\mathrm{p}} + \gamma\gamma + Z \rightarrow \bar{\mathrm{p}} + e^+ + e^- + Z \rightarrow \bar{\mathrm{H}} + e^- + Z \tag{3.1}$$

The first production took place at the experiment JETSET, which modified its target to spray a Xe (with high-Z) jet into the path of the circulating antiprotons and added a detection system after the straight section of LEAR in order to detect formed $\bar{\mathrm{H}}$. The experiment observed 9 antihydrogen atoms moving at 90% of the speed of light [21].

3.2 Production of cold antihydrogen by three-body recombination

On the other hand, a collaboration TRAP investigated the production of cold antihydrogen by three-body recombination:

$$\bar{\mathrm{p}} + \mathrm{e}^+ + \mathrm{e}^+ \rightarrow \bar{\mathrm{H}} + \mathrm{e}^+ \tag{3.2}$$

In this process, the recombination rate increases with the square of the e^+ density and it is proportional to $\mathrm{T}^{-9/2}$, where T is the temperature of e^+.

Shortly after capturing the first antiprotons, in 1986 [22], a new form of production of a cold antihydrogen was proposed. The idea is based on the principle of so-called nested (double well) trap, which is a trap divided into two potential wells (the central and the outer one). Cold positrons are loaded into the central well and antiprotons are loaded in the outer one. Then, antiprotons are launched into the central well, they slow down by loosing energy via collisions with positrons and form antihydrogen.

However, the development of an efficient accumulation took a lot of time. The simultaneous trapping of e^+ and $\bar{\mathrm{p}}$ was achieved in 1996 [23] and the first positron cooling of antiprotons in 2000 [24].

In 1996, when the LEAR was closed and the new decelerator (AD) was approved, second generation of experiments (ATHENA and ATRAP) formed with a goal of producing cold antihydrogen atoms. In August 2002, ATHENA was the first experiment to observe cold antihydrogen atoms [25].

The configuration of the nested trap used to produce antihydrogen can be seen in Figure 3.1. Antiprotons are launched into the positron plasma by a short pulse from the solid to the dashed potential and then oscillate back through the cold positrons. Therefore they loose energy via Coulomb collisions and when they reach a low relative velocity, formation of the antihydrogen is expected.

As a confirmation of the mechanism of production, (A)TRAP observed the antihydrogen atoms only 6 weeks later [26].

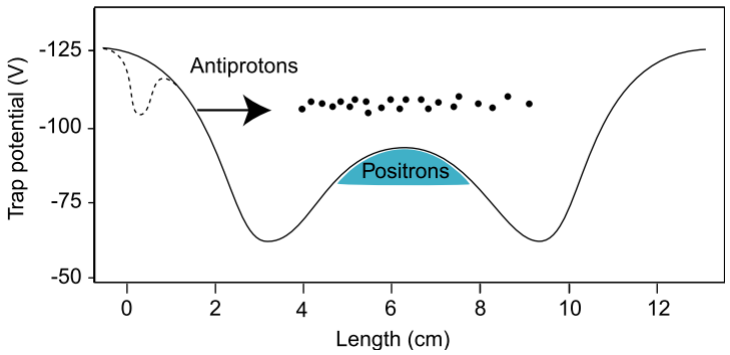

Figure 3.1: The configuration of the field in the nested trap. Positrons are stored in the trap. Antiprotons are launched into the positron plasma by a short pulse from the solid to the dashed potential and then oscillate back through the cold positrons. Taken from [25].

3.3 Production of cold antihydrogen using resonant charge-exchange

Another type of production of $\bar{\mathrm{H}}$ uses collisions between $\bar{\mathrm{p}}$ and excited Ps atoms:

$$\mathrm{Ps}^* + \bar{\mathrm{p}} \rightarrow \bar{\mathrm{H}}^* + \mathrm{e}^-, \tag{3.3}$$

where * stands for a high excited Rydberg state.

This reaction has the following advantages:

1. The cross section scales as $\sigma \propto n_{Ps}^4$, where $\mathrm{n_{Ps}}$ is the positronium principal quantum number. The plot of this dependence can be seen in Figure 3.2.

2. The temperature of the formed antihydrogen is given by the temperature of incoming antiprotons.

3. The principal quantum number of antihydrogen ($\mathrm{n_{\bar{H}}}$) is determined by the quantum state $\mathrm{n_{Ps}}$ of positronium that formed it: $\mathrm{n_{\bar{H}}} = \sqrt{2} n_{Ps}$.

The first formation of antihydrogen atoms using a charge-exchange was demonstrated by the experiment ATRAP in 2003 [27]. In this experiment, a beam of Cs atoms is directly excited by lasers to high Rydberg state, Cs*. Then, two resonant charged exchanged collisions

$$\mathrm{Cs}^* + \mathrm{e}^+ \rightarrow \mathrm{Ps}^* + \mathrm{Cs}^+ \tag{3.4}$$

$$\mathrm{Ps}^* + \bar{\mathrm{p}} \rightarrow \bar{\mathrm{H}}^* + \mathrm{e}^- \tag{3.5}$$

transfer the Cs* binding energy to excited positronium atom and then to excited $\bar{\mathrm{H}}$.

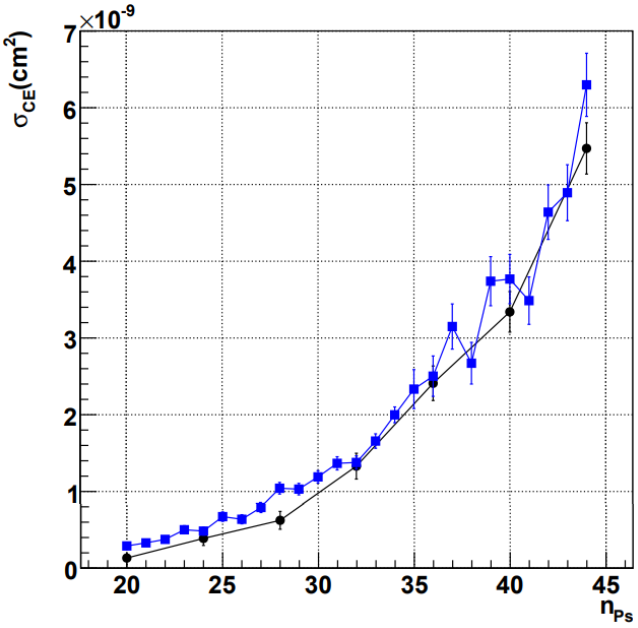

Figure 3.2: The cross section of the antihydrogen production depending on n_{Ps}. Blue squares stand for randomly choosen l and black point for $l = 2$, where l is Ps orbital quantum number. Taken from [28].

The schematics of the formation can be seen in Figure 3.3. The apparatus consists of three Penning traps (yellow regions) for positrons, antiprotons and for formed antihydrogen. At first, Cs atoms from an oven are excited with two lasers. Then they reach the positron trap in order to form Ps atoms (Eg. (3.4)). After that, some fraction of the Ps enters the antiproton trap and produce $\bar{\mathrm{H}}$ (Eq. (3.5)). A small fraction of these atoms reaches the detection trap, where they could be detected.

Due to small solid angles and not enough trials, only 14 ± 4 $\bar{\mathrm{H}}$ atoms were detected, which correspond to 100-200 $\bar{\mathrm{H}}$ produced [27].

Another experiment, which wants to use a resonant-charge exchange to produce antihydrogen is called the GBAR experiment (Gravitational Behaviour of Antihydrogen at Rest) [29]. The aim of this experiment is similar to the AEgIS's one, that means to perform the free fall of antihydrogen atoms and then measure the gravitational acceleration of antimatter on Earth. The idea of the experiment is to use $\bar{\mathrm{H}}^+$ ions, which can be cooled easier than the neutral atoms. The cooling is based on the sympathetically cooling with laser cooled matter ions (Be^+) and the final temperature of $\bar{\mathrm{H}}^+$ should be less than 10 μK.

The production of the atoms takes place in two steps:

$$\bar{\mathrm{p}} + \mathrm{Ps} \rightarrow \bar{\mathrm{H}} + \mathrm{e}^- \tag{3.6}$$

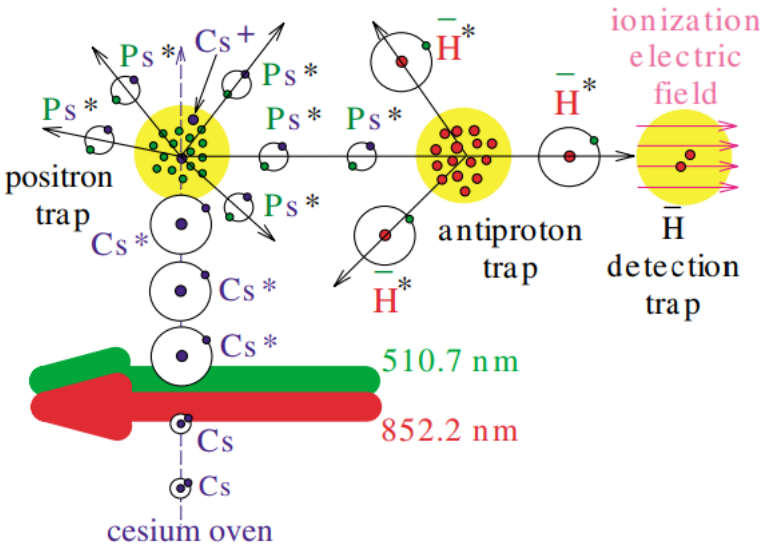

Figure 3.3: The schematics of the antihydrogen production in ATRAP apparatus. Cs atoms from the oven are excited by a group of lasers and then they reach the positron trap in order to form Ps atoms. After that, some fraction of the Ps enters the antiproton trap and produce $\bar{H}$. A small fraction of these atoms reach the detection trap, where they are caught. Taken from [27].

$$\bar{H} + Ps \rightarrow \bar{H}^{+} + e^{-} \tag{3.7}$$

The antiprotons will be provided by the ELENA facility and the positronium will be produced by the implementation of positrons into the nanoporous silica target in a cylindrical shape in order to increase the efficiency of the Ps production.

In Figure 3.4, cross-sections for the reactions (3.6) and (3.7) are calculated for the various state of Ps. As can be seen, the Ps atoms do not have to be excited to a high Rydberg state, which means the production of the atoms is simpler. The excitation of Ps will be provided by a laser with a wavelength of 410 or 243 nm.

It also can be seen, that to the highest cross section leads the state Ps(2p) and the impact energy around 2 keV. Also, to obtain a reasonable number of atoms the energy of the antiprotons should be below 5 keV (ELENA provides $\bar{p}$ with the energy of 100 keV). The cooling of the antiprotons is performed by using a drift tube.

The GBAR experiment aims to produce 1 trapped $\bar{H}^{+}$ per ELENA cycle (100 s).

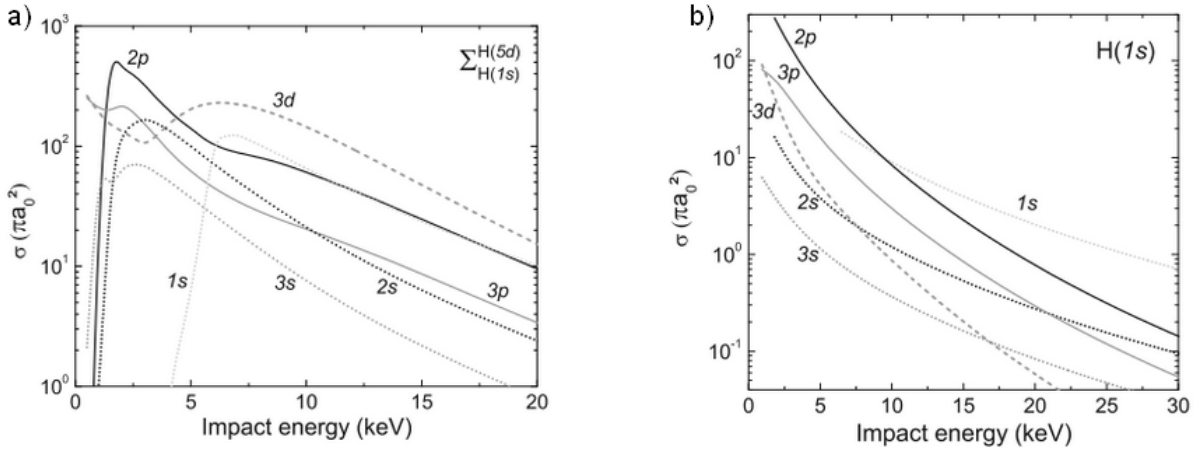

Figure 3.4: The cross sections for the antihydrogen production in the GBAR experiment for various state of Ps and various impact energy of antiprotons. a) for the reaction (3.6); b) for the reaction (3.7). Taken from [30].

Chapter 4

2018 beamtime: Antihydrogen Production in AEgIS

In the AEgIS experiment, antihydrogen is produced via three-body charged recombination:

$$Ps^* + \bar{p} \rightarrow \bar{H}^* + e^- \tag{4.1}$$

As can be seen from this equation, for a successful formation two components are needed: positronium in a high excited Rydberg state and cold antiprotons. The most important results of manipulation of antiprotons, which leaded to the successful conditions will be described in this chapter together with the production itself.

4.1 Preparation of antiprotons

As the temperature of formed antihydrogen depends on the temperature of incoming antiprotons, the aim is to have as cold antiprotons as possible. To the cooling, compressing and stacking of the antiproton plasma were dedicated beamtimes in years 2014-2017 and most of the results can be seen in [31].

The preparation of $\bar{\text{p}}$ plasma in the 5 T region is divided into five steps. As of the time of writing, the only performed cooling of antiproton plasma is by collisions with electrons and the compression is achieved by the rotating wall effect. All the steps can be seen in Figure 4.1.

4.1.1 Antiproton loading, cooling and compression in 5 T region

At first, electrons are loaded and prepared in the P-trap (for more details see apparatus regions described above). The number of electrons can be changed by changing the trap-

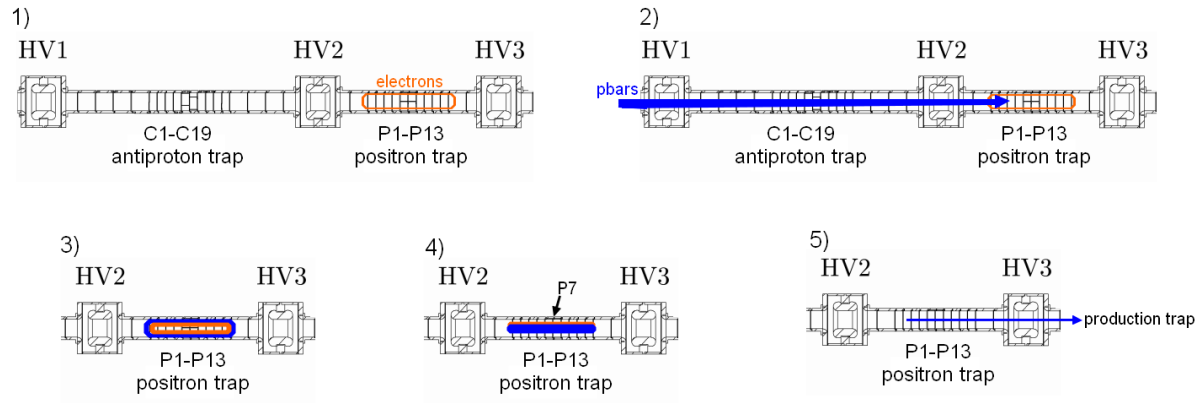

Figure 4.1: The five steps of cooling and compressing antiprotons in 5 T region: 1) loading electrons; 2) loading and degrading pbars; 3) electron cooling; 4) applying RW at P7; 5) transfer to the production trap.

ping voltage (higher voltage means a higher number of electrons). Usually, 10^8 electrons are loaded with a density about 10^8 e^-/cm^3.

Then, antiprotons from AD are loaded. Immediately after the arrival in the apparatus, they are slow down firstly by a (53 ± 3) μm thick silicon beam monitor and secondly by a (173.7 ± 0.5) μm thick degrader (an Al foil). As $\bar{p}$ fly throw C-trap, only the low-energy fraction (below 100 meV) is captured. The efficiency of this process is about 1.25%, that means from 1 AD bunch ($3{\cdot}10^7$), $3.7 \cdot 10^5$ antiprotons are captured. After that, both plasmas are mixed together in the P-trap. This trap is about 35 cm long, has a radius of 1.5 cm and the end-cap voltage is set to 9 kV.

Next, the electron cooling of antiprotons via collisions takes place in P-trap. The energy is lowered from ~keV down to ~eV (and lower) range with the cooling time lower than 50s. After that, the end-caps electrodes are grounded and therefore the non-cooled antiprotons are released towards the degrader, where their number can be measured. The efficiency of the electron cooling is about 50-60%, which means the final number of $\bar{p}$ after the cooling process is $\approx 2 \cdot 10^5$ $\bar{p}$.

When the antiproton plasma is cooled down, it needs to be compressed, which is performed by a Rotating Wall technique by using four-sectored P7 electrode. It was observed, that the compression dynamics for a pure electron plasma is the same for the mixed plasma. The key experimental condition is the one, in which antiproton density distribution follows the electron one. Then, the mixed plasma is radially compressed to 0.2 mm with the efficiency around 45%.

The key detection mechanism for compressing charged particles is the MCP coupled to a Phosphor screen and read by a CMOS camera, which is mounted at the end of the

apparatus behind the 1 T region.

Also, the centrifugal separation between electrons and antiprotons was observed; the image from the MCP can be seen in Figure 4.2. However, it is important to work in such a condition when this separation is avoided because under these circumstances, only electron plasma is compressed and antiprotons stay at large radii.

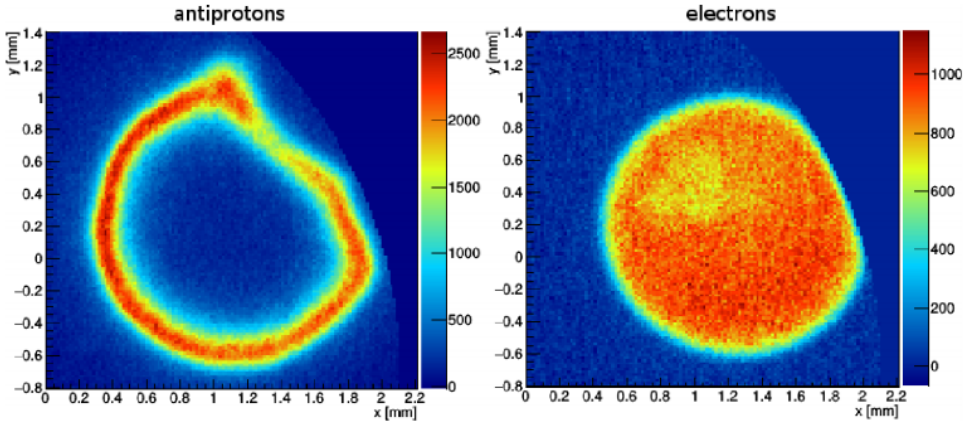

Figure 4.2: Images from the MCP for identical particle operations with antiproton detection (left) or electron detection (right). The centrifugal separation effect between electrons and antiprotons with no antiprotons compression is clearly visible. Taken from [31].

In the 5 T region, more than 1 AD bunch can be stored. During the year 2018, the stacking of a larger number of shots was investigated and the linear trend was observed (can be seen in Figure 4.3). The MCP images from the procedure of stacking 1 to 5 pulses can be seen in Figure 4.4. Usually, 8 AD shots can be stored without no significant losses, which correspond up to 10^6 antiprotons.

Finally, the plasma is transferred into the production trap with efficiency around 80%. Before 2016, a procedure called "adiabatic transfer" was used. The principle of this procedure was the shift of the mixed plasma by changing the voltage on the trap electrodes, from the 5 T region to the 1 T one. However, the efficiency of this procedure was limited by a misalignment between the two magnets. Since 2016, a procedure called "ballistic transfer", which re-catch in-flight only the antiproton cloud, is used for the transfer. The catch of the antiprotons is achieved by setting the end-cap potential to 0 V in five 80 ns long pulses and thus allows the electrons to escape whiles the majority (90%) of antiprotons remains trapped. The advantage of this procedure is the availability of setting a static voltage to the electrode which is mounted in the transition region between the magnets and thus apply the controlled shift of the radial position of the antiproton plasma. Also, the procedure allows transferring the plasma with only with the expansion

caused by the decrease of the magnetic field. The MCP images with no correction and with the best setting (correction and also centering) can be seen in Figure 4.5.

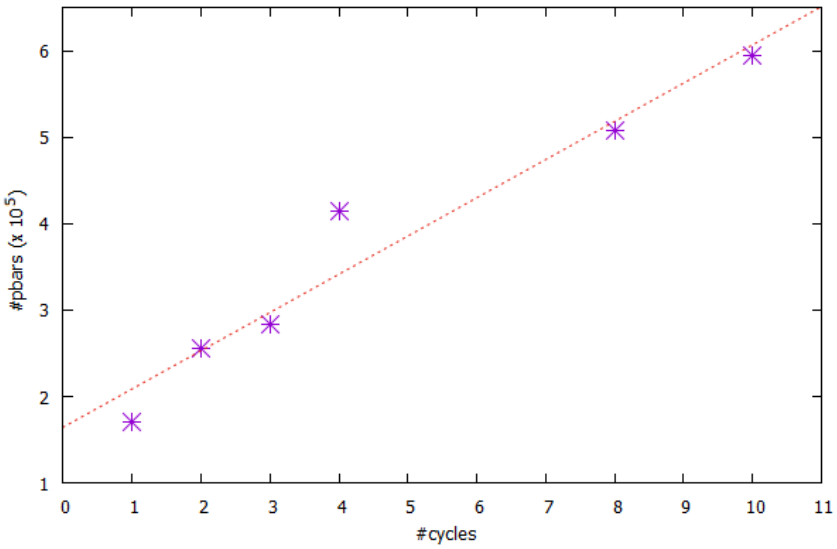

Figure 4.3: The number of stacked antiprotons versus the number of AD shots. The linear trend of stacking can be seen.

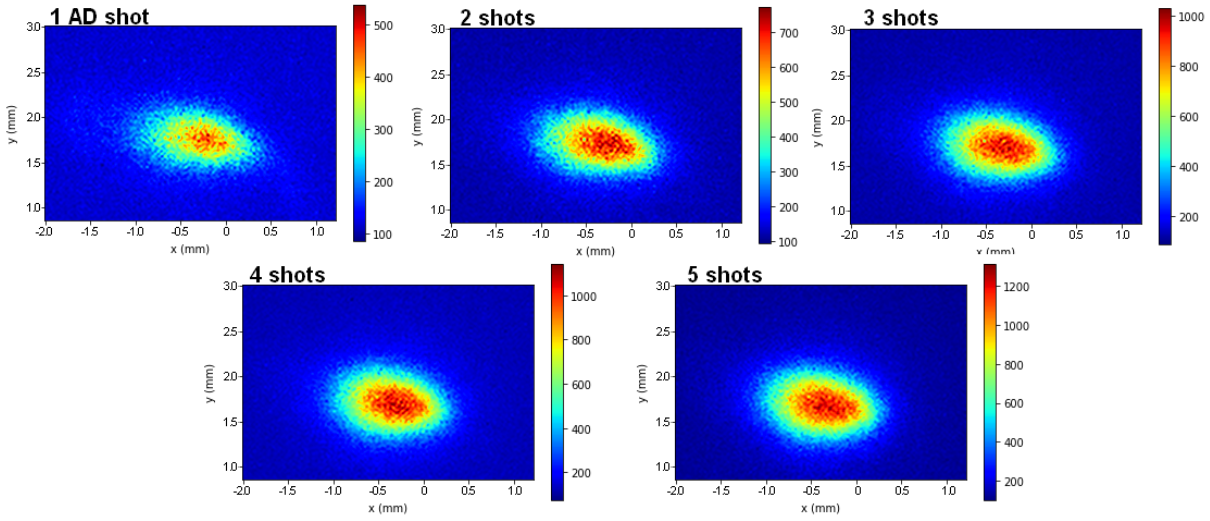

Figure 4.4: Evolution of the antiproton cloud during stacking 1-5 AD shots. The size of the cloud remains in the same shape, only the intensity is getting higher with every shot.

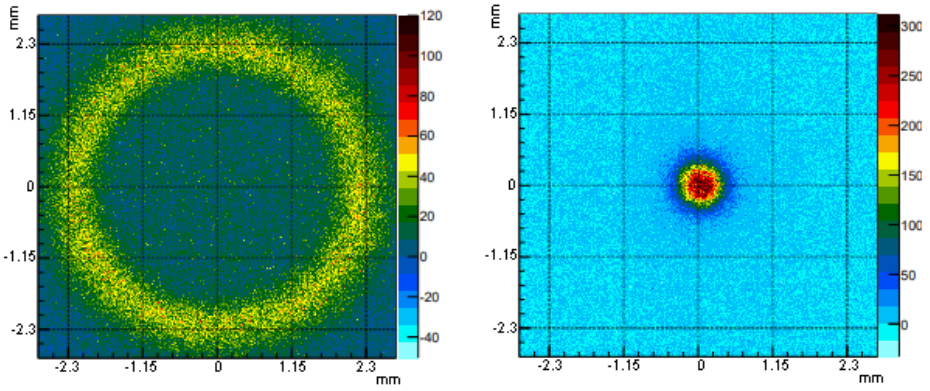

Figure 4.5: Images of the antiproton plasma from the MCP. Antiprotons were launched from the 5 T region into the production trap, stored there for 1 ms and then dumped on the MCP. a) the image without any correction; b) best setting of the correction and centering.

4.1.2 Antiproton cooling in the 1 T region

In the 1 T region, antiprotons need to be cooled again. As most of the electron from the 5 T region is lost during the ballistic transfer (due to their higher velocity), for the cooling new electrons need to be loaded. Since it is difficult to load them immediately from the 5 T region into the 1 T, they are loaded into the 5 T, cooled down, compressed and then adiabatically transferred into the Big trap in the 1 T magnet where they are re-compressed with a Rotating Wall. Due to a huge storage time of electrons (many hundreds of seconds), they can wait in the Big trap for incoming antiprotons and then they can be ballistically transfered into the production trap, where are the antiprotons cooled. Usually, about $3 \cdot 10^7$ electrons are loaded into the 1 T trap and the cooling last for a few tens of seconds. After that, Rotating Wall is applied to compress the mixed plasma a then the number of electrons is reduced by a fast voltage pulse at the end-caps electrodes.

Mixed plasma is then shifted to the selected electrode (UC1-15) potential well. With 8 AD shots the final number antiprotons is about $8 - 9 \cdot 10^5$ trapped with $5 \cdot 10^5$ electrons. The lowest temperature was achieved by using a trap between electrodes UC2-UC6, $T = (237 \pm 21)$ K. However, this region is not suitable for antihydrogen production (the Ps target is mounted above the electrode UC8), so during the year 2018 the temperature in the region between the electrodes UC4-UC8 was measured with the result $(T = 440 \pm 80)$ K.

The mixed plasma in the production trap can be stored for quite a long time. After

3000 seconds, still a fraction of about 75% of the initial number of antiprotons can be detected with almost no plasma expansion.

As mentioned before, the main detector used for determination of the shape and position of both types of plasma is the MCP, which measures the radial density profile integrated along the magnetic field axis and is placed at the end of the apparatus at the temperature of 40 K. However, due to its long dead-time (60 ms), it could not be measured at once both of the radial profiles (antiprotons and electrons). To obtain both MCP images, each experiment is repeated in the same conditions once with the $\bar{p}$ image and once with the e^- image.

On the other hand, external scintillators are used to determine the number of antiprotons from the number of annihilations on the degrader foil placed at the different places in the experimental apparatus. For the incoming, not cooled $\bar{p}$ (so-called Hot Dump), usually scintillators SC34 are used, as they are placed around the P-trap. For the number of cooled antiprotons (so-called Cold Dump), scintillators SC2122, placed around the production trap are used. To see the exact place, where the scintillators are mounted, see the chapter 2. The typical result from the scintillator, the number of events in a selected time window, is shown in Figure 4.6.

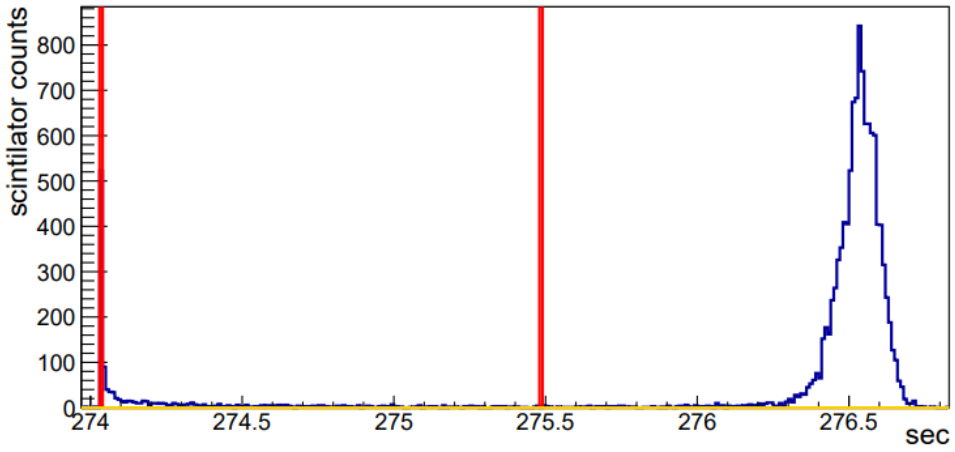

Figure 4.6: Time distribution of the annihilation of antiprotons in the 1 T region. The first red mark shows the time when the pulse used to re-catch in-flight antiprotons is applied. The second red mark indicates the beginning of the ramp of the voltages used to dump and count the antiprotons. The peak corresponds to about $2 \cdot 10^5$ antiprotons.

4.2 Antihydrogen production

When (cold) antiprotons are prepared in the production trap and the laser for exciting Ps cloud is set, the antihydrogen production itself can be started. As mentioned above, this type of production is pulsed, that means we can divide it into cycles. One antihydrogen cycle corresponds to 100 second, during which a given amount of positron pulses is accumulated in the accumulator (typically 420 pulses) and then send to the main trap, being excited and passed through the mixed plasma in the production trap. Under standard conditions a production procedure of 24 cycles guaranteed a good reliability, efficiency and stability (no significant losses of antiprotons). After given amount of cycles, electron plasma is dumped to the MCP and the antiprotons annihilate at the trap's walls. The highest number of cycles without any significant losses or radial expansion of the plasma is 50, which correspond to 75 minutes. The MCP images of the electrons dumped from the antihydrogen production trap after different number of shots and antihydrogen cycles are shown in Figure 4.7. As can be seen, the shape, the size and also the position strongly depend on the conditions, as the radius and the position for almost the same initial parameters (8 shots and 20 (21) cycles) differs.

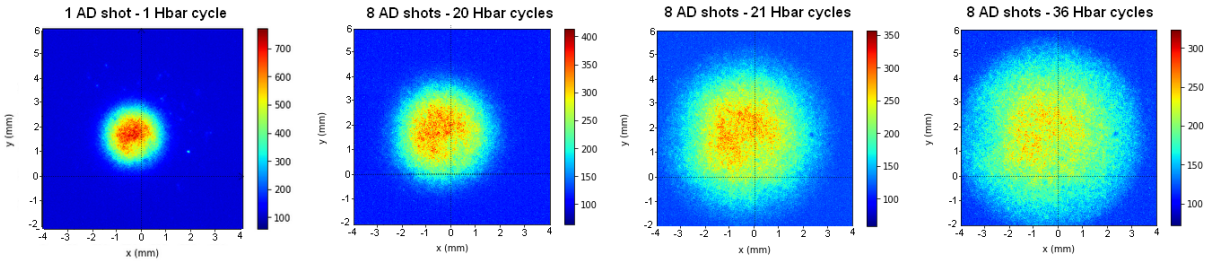

Figure 4.7: The MCP electron image for different number of the Hbar cycles.

The acquired data had to take into account all the possible background. Therefore, five different types of data set was taken (list of them can be seen in Table 4.1).

At first, the conditions for a successful antihydrogen production were given (Hbar ON), which means the antiprotons with the positrons were loaded and also the laser was turned on. During the first stage of the production (during August), the production took place between the electrodes UC6 and UC10 (as the target is placed above the electrode UC8). However, during the second stage of production (during October and November), a region between the electrodes UC4 and UC8 was used and it appeared to be more convenient. The schematics of these two regions is shown in Figure 4.8.

Next data set which was taken, is the measurement with antiprotons, positrons, but with the laser turned off (Hbar OFF). In order to keep the same conditions, one procedure

alternate three types of measurement: ON, OFF and ON again (to gain the ratio 2:1). Usually, with the same antiproton cloud, 21 cycles (14 ON and 7 OFF) were taken.

The next background data were taken by shining the laser while antiprotons were trapped in the production trap, but without any positrons (Background). This measurement should evaluate the effect of a possible background due to desorption of gases during the pulsed laser illumination of the vacuum chamber inner surface.

Next, the data with shining the laser at the positrons, but without antiprotons in the trap were taken to measure the background caused by the excitation of Ps (Positrons).

Last in the list, a cosmic background was taken with a presence of no particles in the apparatus (Muon).

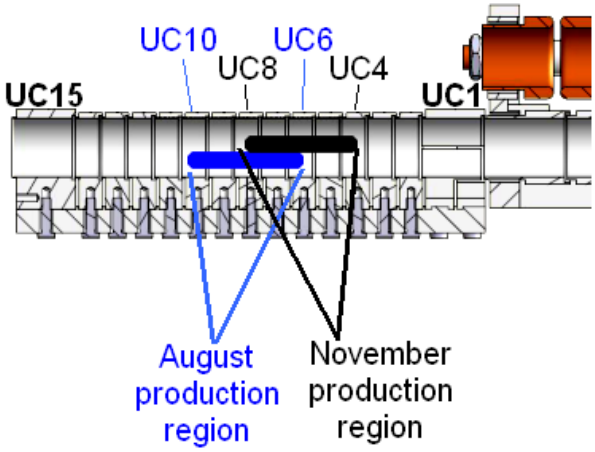

Figure 4.8: Two regions of the Hbar production. The Ps target is placed above the UC8.

data set	pbars	positrons	laser	#cycles
Hbar (ON)	√	√	√	2292
Hbar (OFF)	√	√	×	1250
Background	√	×	√	2995
Positrons	×	√	√	2074
Muon	×	×	×	12360

Table 4.1: Types of datasets taken during the Hbar production together with the number of cycles.

4.3 Antihydrogen detection

The experiment uses two systems to detect the formed antihydrogen - The Fast Annihilation Cryogenic Tracking detector (FACT), which was develop by the collaboration and

the signal from the scintillators placed around the main chamber. Both detectors were briefly described in the section 2.3.

4.3.1 The Fast Annihilation Cryogenic Tracking detector (FACT)

4.3.1.1 Detector

FACT is a scintillating fibre-based detector, which is placed immediately around the production trap (inside the inner vacuum chamber). The detector has three main purposes: to detect antihydrogen, to measure its temperature and to form an antihydrogen beam. The first time, when it was used as a diagnostic tool was during the year 2017.

From the hardware point of view, it has three main requires: it must be very fast in order to identify the hundreds of annihilations in the 1 ms period during the production, it needs to be able to operate at the temperature of 4 K inside a very strong magnetic field (1 T) and finally, it cannot produce more than 10 W of heat.

There are also requirements for the size of the detector: it must operate inside a cylindrical volume with an inner radius of 68 mm and outer radius of 103 mm (this space can be seen in Figure 4.9a).)

In light of these requirements a design based on scintillating fibres with silicon photomultiplier readout was chosen and more details about the construction can be seen in [11].

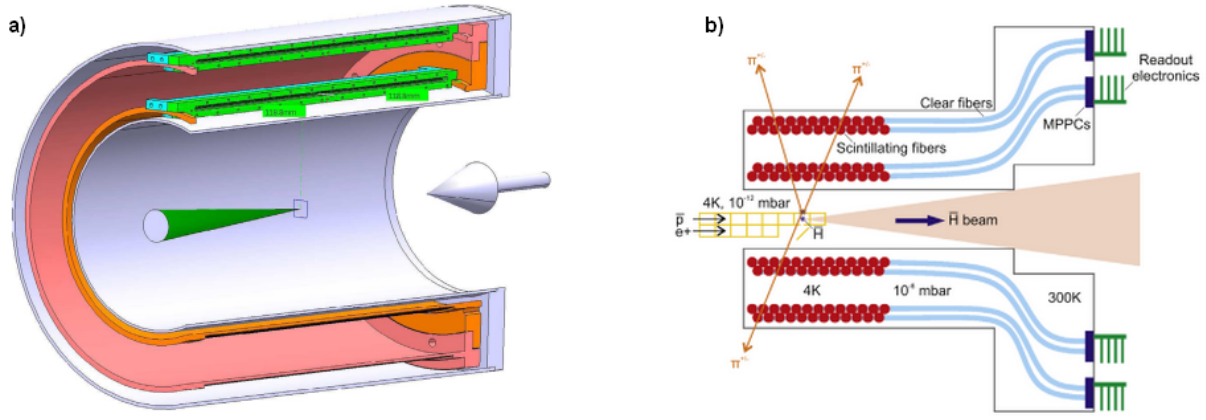

Figure 4.9: Schematics of the FACT detector. a) Section view of the design for the scintillating support structure and the fibre connector. The antihydrogen beam is indicated as a green cone. b) Arranging of the scintillating fibres in the detector. Taken from [11].

4.3.1.2 The principle of detection

FACT is a detector with a vertex reconstruction capability which can be computed if a coincidence appears. An example of a coincidence in the FACT detector is shown in Figure 4.10 left. On the right, an example of the vertex reconstruction can be seen.

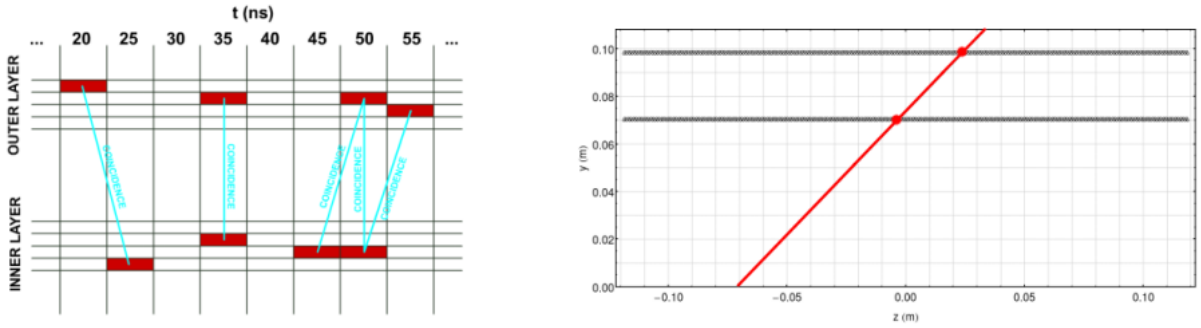

Figure 4.10: Coincidence in the FACT detector. Left: an event is called the coincidence, if the particle hits two same (or neighbouring) fibres in each layer in a given time. Right: an example of the vertex reconstruction for the coincidental event.

When the antihydrogen is produced, at first, positrons are injected into the Ps target. The injection emits a huge number of gamma rays, which "blinds" the detector for a certain time (500 ns). Due to this fact, a fast fraction (energies in order of eV) of the produced antihydrogen atoms cannot be detected by this detector.

Cold antihydrogen atoms are detected by comparing normalized numbers of tracks and vertices in FACT in a later time after the arrival of the positrons for two types of cycles: first, the ones with laser on (when the antihydrogen production is expected) and the background ones (types of background measurements are mentioned above).

Figure 4.11 shows a typical signal from FACT during the antihydrogen production cycle. The positron arrival is at the time t=0. From the signal can be clearly seen the "blind" time, when the detection of antihydrogen atoms is impossible (responds to the time window $0.4 - 2\ \mu s$). This positron burst typically lasts until 8 μs (the second time window). After that, until 20 μs, a signal from the slow antihydrogen fraction can be detected (the third time window) - this region is called as a trackable one. As can be seen from the plots, the distribution of the events is wide with a random noise (mostly caused by fake reconstructed events) and most of the events originated in the center of the production trap (z=0).

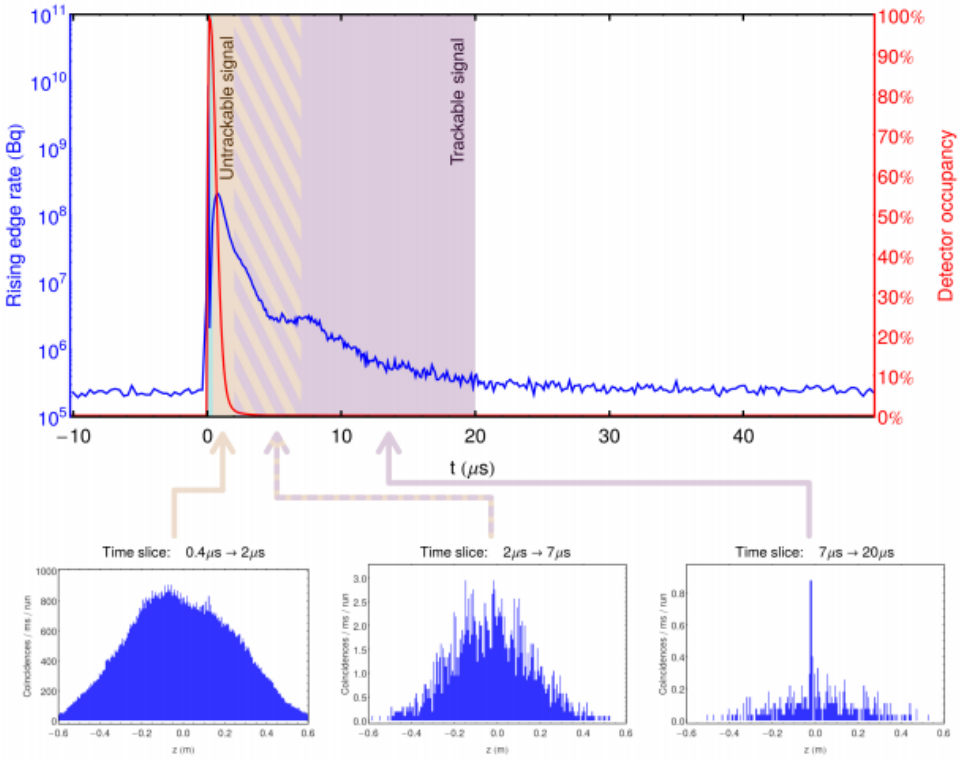

Figure 4.11: FACT signal around the implementation of positrons. The positron arrival is at the time t=0. The "blind" time (responds to the time window $0.4 - 2$ μs) can be clearly seen. This positron burst typically lasts until 8 μs (the second time window). Until 20 μs, a signal from the slow antihydrogen fraction can be detected (the third time window) - this region is called as a trackable one. Taken from [33].

4.3.2 Detection based on scintillators

Due to the limitations of the FACT detector mentioned above, a second detection system based on the scintillating detectors was implemented in 2018 in order to complement it.

All scintillators and their position can be seen in Figure 4.12. For detection of the antihydrogen formation, scintillators around the 1 T magnet were used (in total 11 scintillator slabs). For each slab, the full pulse shape was digitized, which allowed to distinguish between the real pulse and PMT noise.

The overall solid angle of this type of detector array is around 40%, however, the efficiency for a particle traversing any part of the field is close to 100%. That means, the overall detection efficiency is lower than with the FACT, but the signal is cleaner.

Every scintillator slab is connected to 2 PMTs. As a signature of a passage of a particle, a presence of a peak above a given threshold in both PMTs is taken into account. The spectrum from the scintillators are then the sum of these peaks amplitudes.

The signal can be seen in Figure 4.13. On the left, a spectrum of amplitudes for antiproton annihilations (in 1 T trap) in one slab is shown and on the right, spectrum of amplitudes for single gamma rays produced by positron and positronium annihilation is shown. From the plots is clear, that the threshold for selecting a passing particle is 200 mV per one PMT, that means 400 mV for each scintillator.

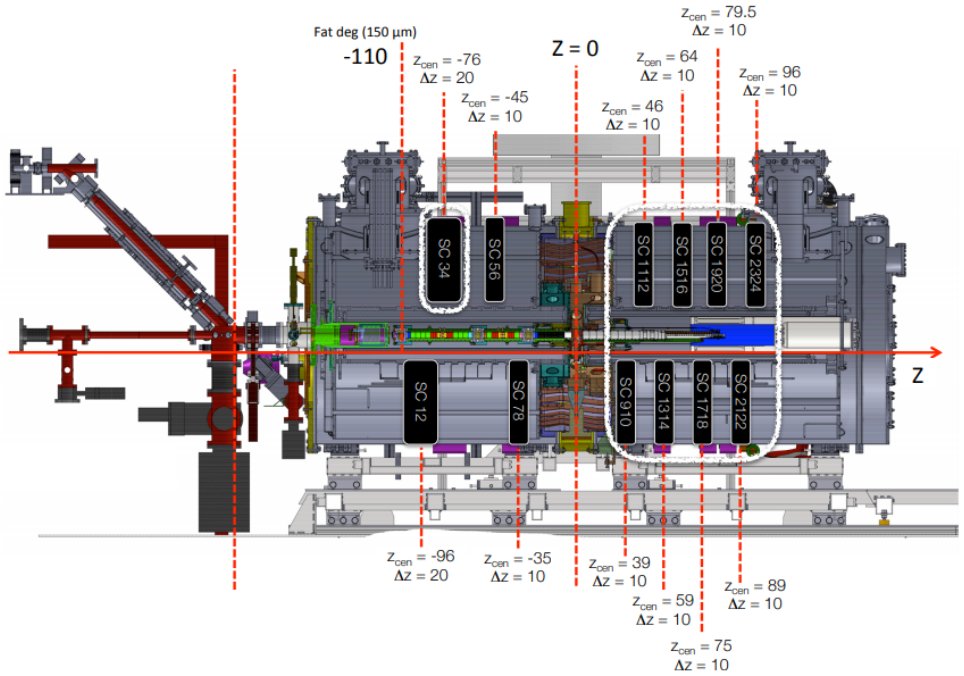

Figure 4.12: The position of all scintillators placed around the main apparatus. The white frame refers to the scintillators, which are used for antihydrogen detection. All measures are in cm.

From the analysis point of view, two types of regions are chosen. First, a control region - time windows, which are important for the background measurements and random antiproton losses. One of the window is before the arrival of the positrons (from -101 μs to -1 μs) and the second window is too late after the arrival (from 51 μs to 551 μs). As a second, a signal region - the time window, where the annihilation signal can be seen, from 1 μs after arrival to 31 μs. For the first microsecond after the arrival of the positrons, the detector is blind because of the large burst of gamma rays (for the FACT, it is 8 microseconds).

The signal of produced antihydrogen is then the difference of the production runs and the background runs in the signal region above the given threshold in a selected time window.

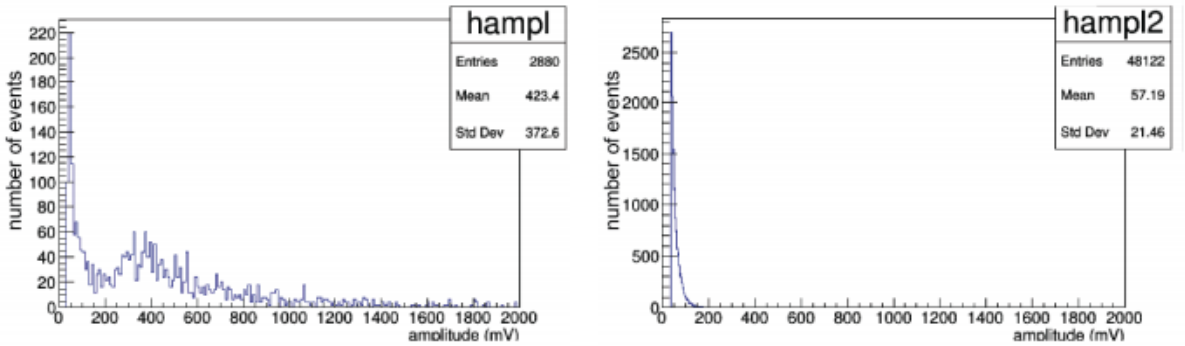

Figure 4.13: Signal from the scintillator. Left: number of events above given threshold during Ps formation antiproton annihilation; right: number of events above given threshold during only Ps formation. Taken from [33].

During the year 2018, a total number of 2292 antihydrogen production cycles and a total number of 18679 background cycles were taken. As of the time of writing, the final conclusion about the antihydrogen production has not been published yet. However, the production mechanism (4.1) was proven to be successful and the collaboration will continue in investigating the possible improvement of it.

Chapter 5

Micro-Channel Plate Image Analysis

The aim of the image restoration is to find the real image, without any noise. The applications of the restoration are in different fields, such an astronomy, optics, seismology and medical imaging. Usually, one get a blurred image, the noise is caused by the atmosphere, by defocusing the camera or inaccuracies in the optic system.

The model of the degradation process is a convolution:

$$(f * g) + \epsilon = h, \tag{5.1}$$

where h is the real (blurred, noisy) image, f is the original image, g is *the point spread function (PSF)* - the function which caused the blurring and ϵ is some kind of added noise.

The restoration of the image can be then divided into two groups. If the process and its noise (the point spread function h) is known, then the restoration is an inverse problem to (5.1) and it is called *deconvolution.* On the other hand, if the PSF g is not know, or there only a little information about it, the process is called *blind deconvolution.*

Deconvolution can be performed by computing the Fourier Transform of the signal h and the PSF g, which change the convolution to a single multiplication:

$$H = F \cdot G, \tag{5.2}$$

from which we can obtain the original signal:

$$F = H/G, \tag{5.3}$$

where F,G and H are the Fourier Transforms of f,g and h.

Finally, by performing an inverse Fourier Transform of F one can find the deconvolved signal f.

In order to improve the original image f, many techniques (Wiener, Maximum A Posteriori - (MAP), Maximum Likelihood Estimation - (MLE), Richardson-Lucy deconvolution) were implemented. In the next sections, the Richardson-Lucy algorithm will be explained more deeply and some examples of the deconvoluted images will be shown.

5.1 Richardson-Lucy blind deconvolution

The Richardson-Lucy (R-L) deconvolution algorithm was derived from Bayes's theorem in the early 1970s [34],[35] and since then it became very popular throughout many fields, such as astronomy and medical imaging. The reason, why this algorithm is so popular is its implementation of maximum likelihood and its ability to produced restored images in a good quality despite the presence of a high noise.

Bayes's theorem is given by:

$$P(x \mid y) = \frac{P(y \mid x)P(x)}{\int P(y \mid x)P(x)dx}, \tag{5.4}$$

where $P(y \mid x)$ is the conditional probability of an event y, given event x. $P(x)$ is the probability of an event x and $P(x \mid y)$ is the inverse conditional probability (of an event x, given event y).

In the case of (de)convolution, the probability $P(x)$ refers to the (original) image distribution f, the conditional probability $P(y \mid x)$ can be identified as the point spread function g and the probability $P(y)$ is the real (blurred) image h.

From this relation, an iterative relation can be derived:

$$f_{i+1}(x) = f_i(x) \int \frac{g(x,y)h(y)dy}{\int g(y,z)f_i(z)dz}, \tag{5.5}$$

where $i = \{0, 1, \dots\}$ is the iteration number and the initial f_0 is estimated.

The Eq. (5.5) can be rewrite in a terms of convolution:

$$f_{i+1}(x) = f_i(x) \left[\frac{h(x)}{f_i(x) * g(x)} * g(-x) \right]. \tag{5.6}$$

If the PSF (g) is known, the restored (original) image f can be found by iterating (5.6) until it converges.

If the PSF (g) is not known, an algorithm for the blind deconvolution is needed. At the beginning, the initial guess of PSF g is needed. Then, this algorithm assumes, that at the kth iteration the object is already known from the $(k-1)$ iteration. That means, the point spread function $g^k(x)$ can be calculated for a specific number of R-L iterations:

$$g^k_{i+1}(x) = g^k_i(x) \left[\frac{h(x)}{g^k_i(x) * f^{k-1}(x)} * f^{k-1}(-x) \right], \tag{5.7}$$

which is an inverse for Eq. (5.6) and calculate the PSF from the known original image.

Then, f^k is calculated for the same number of iterations with the obtained PSF:

$$f^k_{i+1}(x) = f^k_i(x) \left[\frac{h(x)}{f^k_i(x) * g^k(x)} * g^k(-x) \right], \tag{5.8}$$

The described loop is then repeated until it is required.

5.2 Results obtained by using R-L blind deconvolution

One of the most important diagnostic tool for charged particles in the AEgIS experiment is the micro-channel plate detector (MCP). This detector is placed at the end of the AEgIS main apparatus, behind the 1 T region, which allows the option to obtain images of all particles after they are dumped from the apparatus to the detector. In this section, electron images were analysed.

5.2.1 Results obtained by changing the PSF

At first, the analysis for different initial point spread functions g was done. The assumption throughout whole analysis is the fact, that the PSF is a Gauss function, which is usually used as PSF model for its simplicity. In figures in the whole section, the PSF is called Gauss(size, sigma), which refers to a rotationally symmetric Gaussian low-pass filter of a given size with standard deviation sigma (σ).

In this section, the number of iterations for all restored images was set to 5.

In Figure 5.1, recovered image obtained with the changing of the value parameter in the Gaussian function are shown. The same procedure is then repeated and shown again in Figure 5.2, but for a closer look to the electrons.

In both figures both restored images and recovered PSF (using the R-L algorithm described above) for them can be seen. From the Figure 5.1 can be seen, that the best

value in the Gaussian function is 15 as from with the higher number the image is not recovered well. However, for the closer look the difference is not that clear.

Next step, which was taken, was the changed of the second parameter in the Gaussian function, the standard deviation σ. The results are shown in Figure 5.3. The difference between the restored images and also the recovered PSF is not significant. However, the function for the next analysis was chosen to be Gauss(15,5).

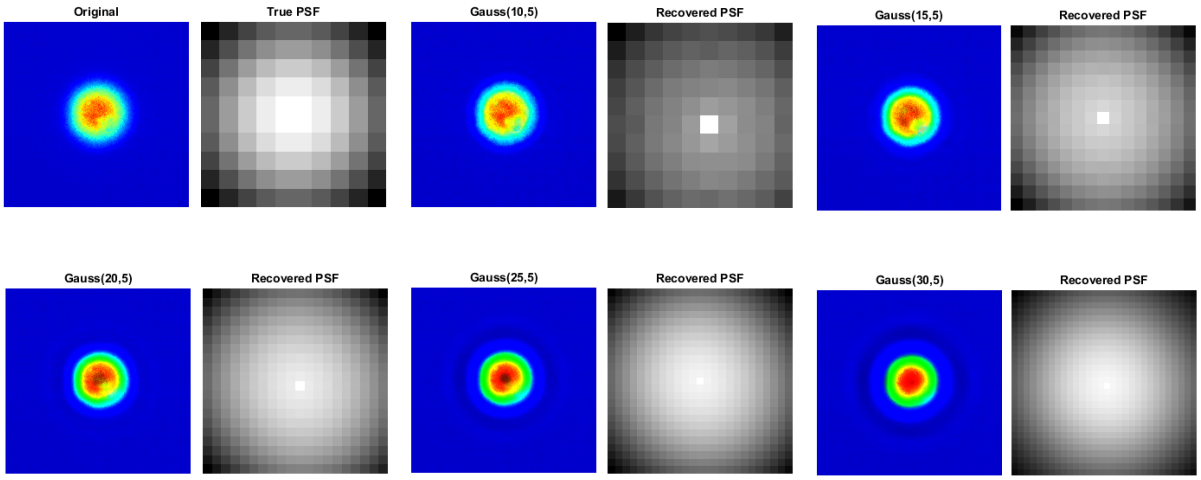

Figure 5.1: Restored images and recovered PSFs for a changing value in the PSF Gaussian function.

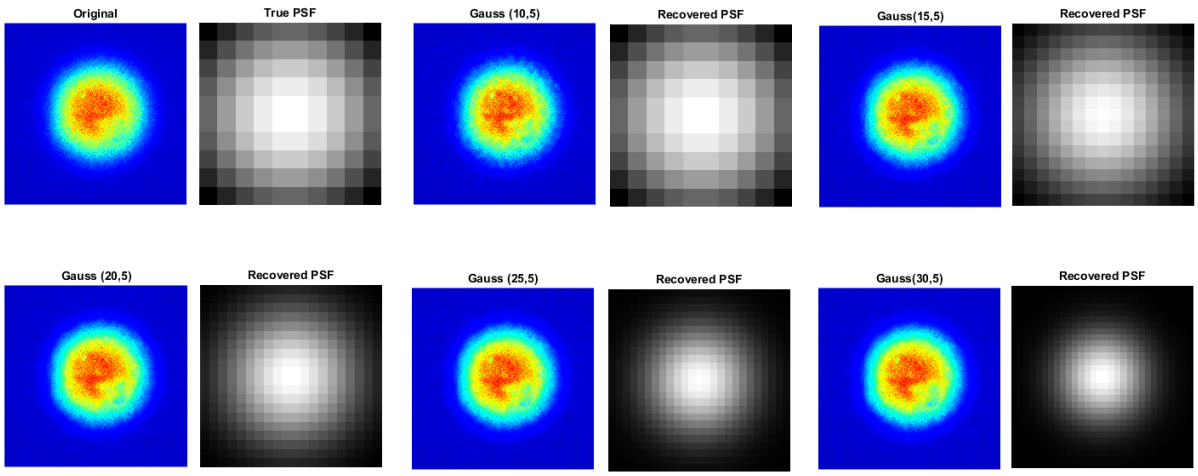

Figure 5.2: Restored images and recovered PSFs (closer electron look) for a changing value in the PSF Gaussian function.

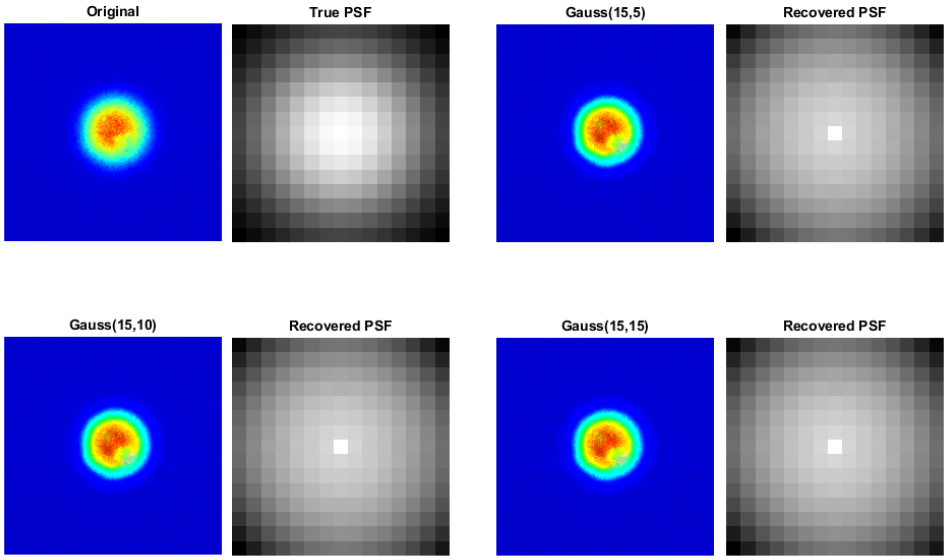

Figure 5.3: Restored images and recovered PSFs for a changing sigma in the PSF Gaussian function.

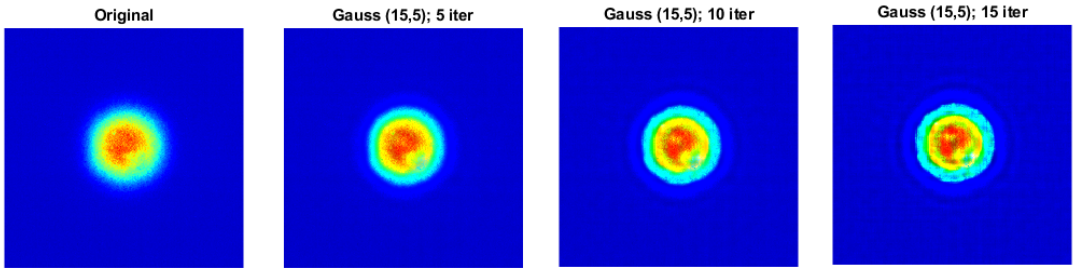

Figure 5.4: Restored images for the iterations with the step of 5. The PSF which was used is Gauss(15,5).

5.2.2 Results obtained by changing the number of iterations

When the initial guess for PSF was obtained, the ideal number of iterations was investigated. In Figure 5.4, a step of 5 iterations can be seen. From the figure is clear, that the ideal number of iterations will be less than 10, since the images for 10 and 15 iterations are not well restored.

Under this assumption, a one step analysis until 10 iterations was done and is shown in Figure 5.5.

After that, the comparison of using the PSF with the standard deviation σ_1=5 and σ_2=10 was analysed for 5 and 10 iterations. The result is shown in Figure 5.6 for an overall look and in Figure 5.7 for the closer look at the electrons. From this figure can be seen, that after 10 iterations, the difference between σ_1 and σ_2 is more significant.

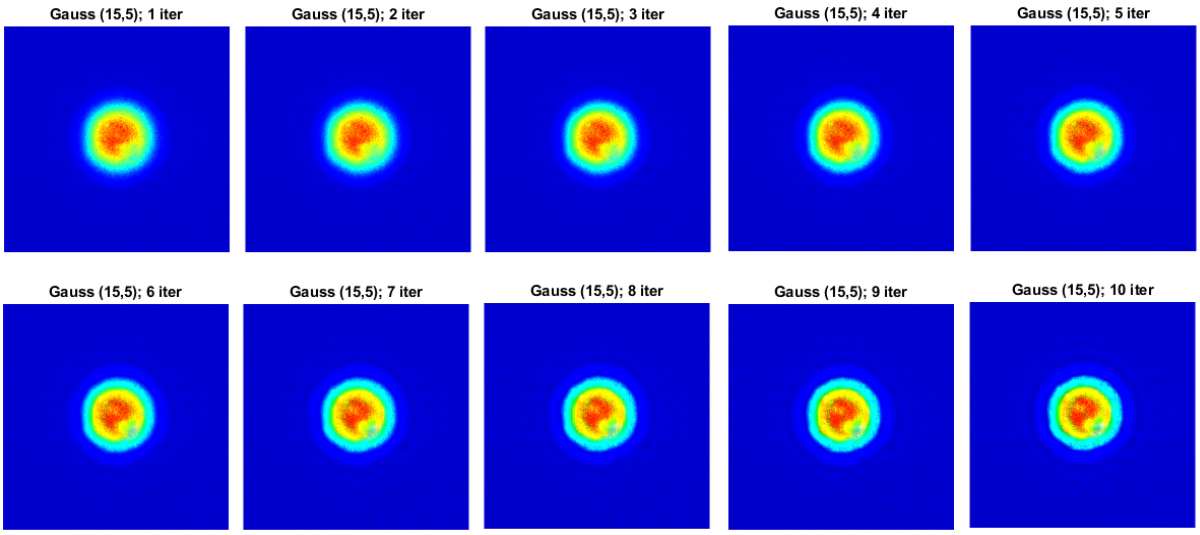

Figure 5.5: Restored images using one step iteration. The PSF which was used is Gauss(15,5).

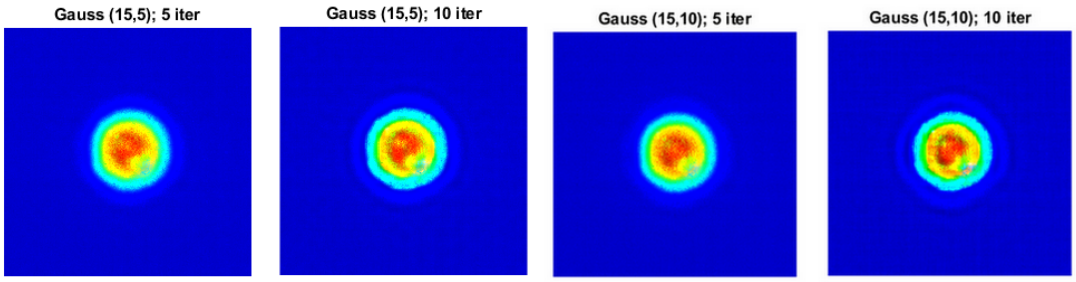

Figure 5.6: The restored images when two types of PSF and 5 or 10 iterations was used.

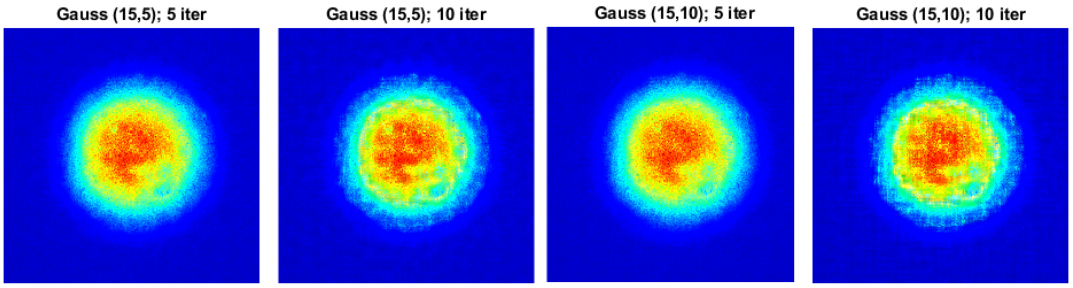

Figure 5.7: Restored images when two types of PSF and 5 or 10 iterations was used (closer electron image).

5.2.3 Deconvolution of the electron expansion

In order to investigate the behaviour of the electron plasma inside the main experimental apparatus, the scan of electron expansion was taken. Its principle is simple: electrons are stored in the 1T for a certain time and then they are dumped to the MCP, where they can be imaged. The expansion from 50 to 800 second can be seen in Figure 5.8 also with the deconvoluted image. For the deconvolution the R-L algorithm with the initial guessed PSF, $f = \text{Gauss}(15, 5)$ and 5 iterations was used.

However, in the figure can be seen, that the image restoration works for smaller electron images (until 400 seconds), but for the larger images is not very successful.

Although the performed deconvolution of the MCP image was successful, some improvements of it would be helpful in the next analysis. At first, a comparison of the radial profiles of both images (real and restored) could help to find the original image. Secondly, the simulation of the optics effects, which blurred the original image would improve the analysis.

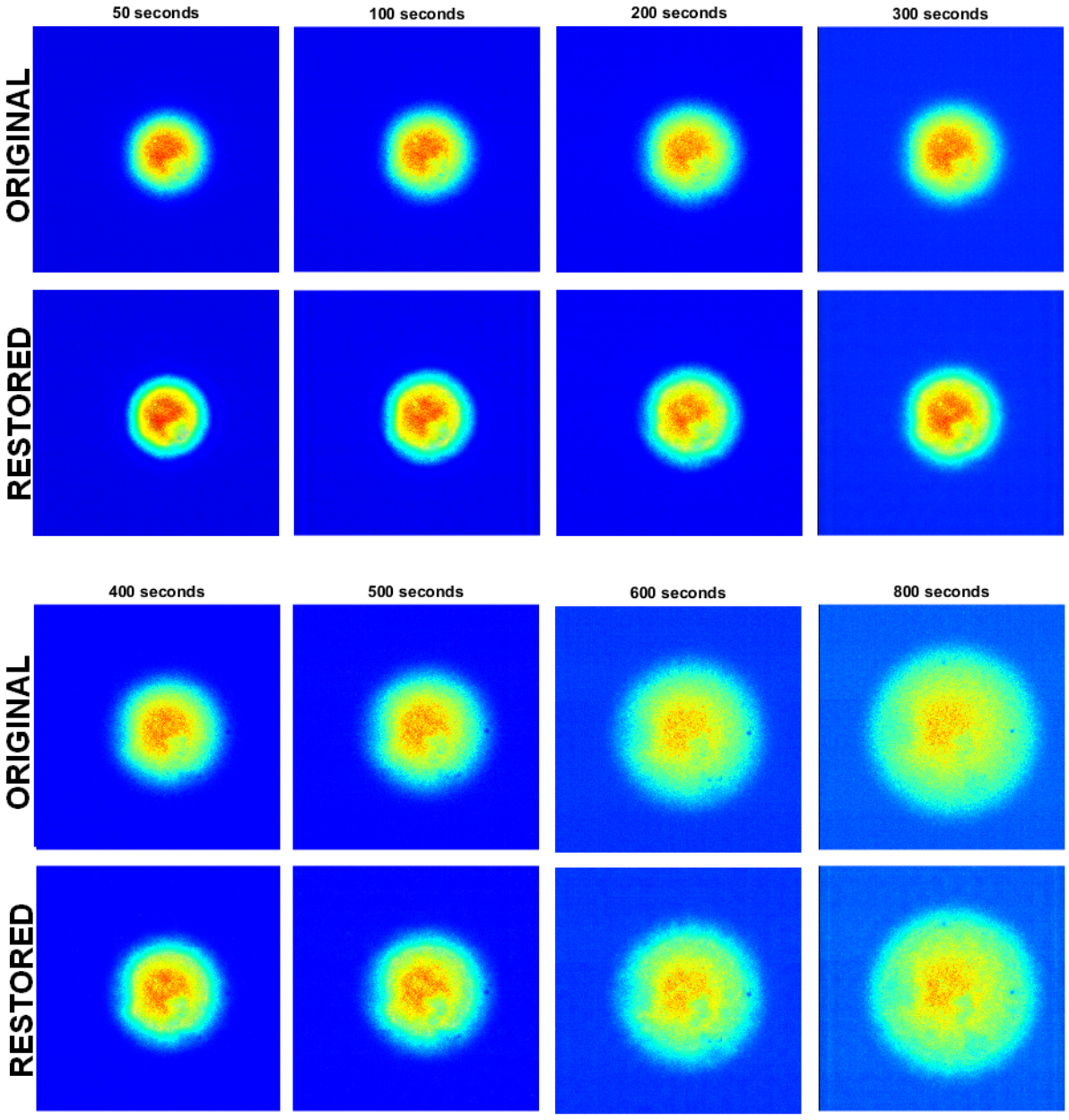

Figure 5.8: Comparison of the original and deconvoluted MCP electron image for the electron expansion. The Gauss(15,5) PSF and 5 iterations was used.

Conclusion

The topic of the thesis is closely connected to the AEgIS experiment, whose collaboration the author joined during the year 2017.

The principal scientific goal of the experiment is to measure the Earth's local gravitational acceleration g on cold $\bar{\mathrm{H}}$ atoms.

The aim of this thesis was to analyse scintillator and image data in order to achieve a successful production of these antihydrogen atoms.

In the first chapter, the theoretical motivation for the measurement of the gravitational acceleration, the Weak Equivalence Principle, was described together with several prior tests of it.

The second chapter was dedicated to the AEgIS experimental apparatus. The hardware layout of the experiment, the positron apparatus and also the heart of the experiment - the main trap apparatus - was described in detail.

Next, different mechanisms for the production of fast, but also cold antihydrogen was summarised.

During the fourth and fifth chapter, the results in which the author took active part were presented. The 2018 beamtime at the AEgIS experiment was dedicated to the antihydrogen production using the resonant charge-exchange mechanism. In this chapter, the most important steps leading to the successful production, together with the main diagnostic tools and data, were shown.

The final chapter of this thesis discussed the improvement of the micro-channel plate images, which are a crucial diagnostic tool. For this purpose, a deconvolution of the image using a Richardson-Lucy algorithm was used.

Bibliography

[1] E. G. Adelberger, J. H. Gundlach, B. R. Heckel, S. Hoedl, and S. Schlamminger: *Torsion balance experiments: A low-energy frontier of particle physics.* Prog. Part. Nucl. Phys, (62):102–134, 2009.

[2] C. M. Will: *The confrontation between general relativity and experiment.* Living Review of Relativity, (17):4, 2014

[3] J. G. Williams, S. G. Turyshev,D. H. Boggs: *Lunar laser ranging tests of the equivalence principle with the Earth and Moon.* Mod. Phys. Lett. A 24, (1129–75), 2009.

[4] A. Einstein: *Zum Relativitätsproblem*, Scientia 15 (337–348), 1914.

[5] Anna M. Nobili, Alberto Anselmi: *Relevance of the weak equivalence principle and experiments to test it: Lessons from the past and improvements expected in space.* Physics Letters A 382, (2205–2218), 2018.

[6] T. A. Wagner, S. Schlamminger, J. H. Gundlach, and E. G. Adelberger: *Torsion-balance tests of the weak equivalence principle.* Classical and Quantum Gravity, (29):184002, 2012.

[7] P. Touboul et al: *The MICROSCOPE experiment, ready for the in-orbit test of the equivalence principle.* Class. Quantum Grav., (29):184010, 2012

[8] A. M. Nobili et al: *'Galileo Galilei' (GG): space test of the weak equivalence principle to* 10^{-17} *and laboratory demonstrations.* Class. Quantum Grav., (29):184011, 2012

[9] ALPHA and A. E. Charman: *Description and first application of a new technique to measure the gravitational mass of antihydrogen.* Nature Communications, 4:1785, 2013.

[10] AEGIS Collaboration: *Probing antimatter gravity – The AEGIS experiment at CERN.* Web of Conferences 126, 2016.

[11] J. Storey et al.: *Particle tracking at 4K: the Fast Annihilation Cryogenic Tracking (FACT) detector for the AEgIS antimatter gravity experiment.* Nucl. Instrum. Methods Phys. Res., Sect. A, 732:437–441, 2013.

[12] *Extra Low ENergy Antiproton (ELENA) ring and its Transfer Lines.*, Design Report, 2014

[13] S. Mariazzi et al. AEgIS experiment: *Towards antihydrogen beam production for antimatter gravity measurements.* Eur. Phys. J. D, 41(68), 2014.

[14] AEGIS Collaboration: *Positron bunching and electrostatic transport system for the production and emission of dense positronium clouds into vacuum.* Nuclear Instruments and Methods in Physics Research B 362, 2015.

[15] AEGIS Collaboration: *Progress report on the AEgIS experiment (2015)*, 2015. `https://cds.cern.ch/record/2121329/files/SPSC-SR-178.pdf` [online 1/4/2019]

[16] S. Berko a H. N. Pendleton: *Positronium.* Annual Review of Nuclear and Particle Science, 1980.

[17] David W. Gidley, Hua-Gen Peng, Richard S. Vallery: *Positron Annihilation as a Method to Charakterize Porous Materials.* Annu. Rev. Mater. Res., 2006.

[18] F. Major , V. Gheorghe , and G. Werth: *Charged particle traps: physics and techniques of charged particle field confinement.* Springer series on atomic, optical, and plasma physics, Springer, Berlin, 2005.

[19] Daniel Krasnický: *Antiproton Capture and Cooling for Production of Cold Antihydrogen.* Ph.D. Thesis, 2013.

[20] Pauline Yzombard: *Laser cooling and manipulation of Antimatter in the AEgIS experiment.* Ph.D. Thesis, 2016.

[21] G. Baur, et al.: *Production of antihydrogen.* Phys. Lett. B 368, 1996.

[22] G. Gabrielse, et al.: *Antihydrogen production using trapped plasmas.* Phys. Lett. A 129, 1988.

[23] G. Gabrielse, et al.: *Precision Mass Spectroscopy of the Antiproton and Proton Using Simultaneously Trapped Particles.* Phys. Lett. B 455, 1999.

[24] G. Gabrielse, et al.: *First positron cooling of antiprotons.* Phys. Lett. B 507, 2001.

[25] M. Amoretti, et al.: *Production and detection of cold antihydrogen atoms.* Nature 419, 2002.

[26] ATRAP Collaboration: *Background-Free Observation of Cold Antihydrogen with Field-Ionization Analysis of Its States.* Phys. Rev. Lett. 89, 2002.

[27] ATRAP Collaboration: *First Laser-Controlled Antihydrogen Production.* Phys. Rev. Lett. 93, 2004.

[28] AEGIS Collaboration: *Proposal for the AEGIS experiment at the CERN Antiproton Decelerator (Antimatter Experiment: Gravity, Interferometry, Spectroscopy)*, 2007. `http://cds.cern.ch/record/1037532/files/spsc-2007-017.pdf` [online 27/3/2019]

[29] P. Perez, et al.: *The GBAR antimatter gravity experiment.* Hyperfine Interact 233, 2015.

[30] P. Comini, P.-A. Hervieux, F. Biraben: $\bar{H}^+$ *production from collisions between positronium and keV antiprotons for GBAR.* Hyperfine Interact 228, 2014.

[31] AEgIS Collaboration: *Compression of a mixed antiproton and electron non-neutral plasma to high densities.* Eur. Phys. J. D 72, 2018

[32] AEgIS Collaboration: *Progress report on the AEgIS experiment (2017)* , 2017. `https://cds.cern.ch/record/2300391/files/SPSC-SR-227.pdf` [online 1/4/2018]

[33] AEgIS Collaboration: *Progress report on the AEgIS experiment (2018)* , 2018. `https://cds.cern.ch/record/2654355/files/SPSC-SR-246.pdf` [online 1/4/2018]

[34] W. H. Richardson: *Bayesian-based iterative method of image restoration.* J. Opt. Soc. Am. 62, 1972.

[35] L. B. Lucy: *An iterative technique for the rectification of observed distributions.* Astron. J. 79, 1974.

[36] D. A. Fish et al.: *Blind deconvolution by means of the Richardson–Lucy algorithm.* J. Opt. Soc. Am. A 12, 1995